# New eastern China agricultural burning fire emission inventory and trends analysis from combined geostationary (Himawari-8) and polar-orbiting (VIIRS-IM) fire radiative power products

Tianran Zhang[1, 2], Mark C. de Jong[1, 2], Martin J. Wooster[1, 2], Weidong Xu[1, 2], Lili Wang[3]

[1] King's College London, Department of Geography, Strand, London WC2R 2LS.

[2] NERC National Centre for Earth Observation (NCEO)

[3] LAPC, Institute of Atmospheric Physics, Chinese Academy of Sciences, Beijing 100029, PR China

*Correspondence to*: Tianran Zhang (tianran.zhang@kcl.ac.uk)

**Abstract**

Open burning of agricultural crop residues is widespread across eastern China, and during certain post-harvest periods this activity is believed to significantly influence air quality. However, the exact contribution of crop residue burning to major air quality exceedances and air quality episodes has proven difficult to quantify. Whilst highly successful in many regions, in areas dominated by agricultural burning MODIS-based fire emissions inventories such as GFAS and GFED are suspected of significantly underestimating the magnitude of biomass burning emissions due to the typically very small, but highly numerous, fires involved that are quite easily missed by coarser spatial resolution remote sensing observations. To address this issue, we here use twice daily fire radiative power (FRP) observations from the 'small fire optimised' VIIRS-IM FRP product, and combine it with fire diurnal cycle information taken from the geostationary Himawari-8 satellite. Using this we generate a unique high spatio-temporal resolution agricultural burning inventory for eastern China for the years 2012-2015, designed to fully take into account small fires well below the MODIS burned area or active fire detection limit, focusing on dry matter burned (DMB) and emissions of $CO_2$, CO, $PM_{2.5}$ and black carbon. We calculate DMB totals 100 to 400% higher than reported by GFAS and GFED4.1s, and quantify interesting spatial and temporal patterns previously un-noted. Wheat residue burning, primarily occurring in May-June, is responsible for more than half of the annual crop residue burning emissions of all species, whilst a secondary peak in autumn (Sept-Oct) is associated with rice and corn residue burning. We further identify a new winter (Nov-Dec) burning season, hypothesised to be caused by delays in burning driven by the stronger implementation of residue burning bans during the autumn post-harvest season. Whilst our emissions estimates are far higher than those of other satellite-based emissions inventories for the region, they are lower than estimates made using traditional 'crop yield-based approaches' (CYBA) by a factor of between 2 and 5x. We believe that this is at least in part caused by outdated and overly high burning ratios being used in the CYBA approach, leading to the

32 overestimation of DMB. Therefore we conclude that that satellite remote sensing approaches which adequately detect

33 the presence of agricultural fires are a far better approach to agricultural fire emission estimation.

34

35 **Keywords**: Agriculture, Biomass Burning, Active Fire, VIIRS, Air Quality, Fire Emission

36

## 1. INTRODUCTION

38 Eastern China (111 - 123 °E, 27 – 40 °N) is home to around one third of the Chinese population and includes the area

39 of the North China Plain and the Yangtze Plain - two of the largest agricultural zones in China (Fig. 1). Cropland

40 covers over 1.7 million $km^2$ of eastern China, and the region is responsible for an estimated 25% of China's crop

41 production, including around 51% of the national rice yield (NBSC, 2012). Large amounts of crop residue (~ 60

42 Tg/year including stems, stalks, straw etc) results from this agricultural production (Chen et al., 2017; Huang et al.,

43 2012; Zhang et al., 2015), and the burning of this waste in open fields is widespread across much of eastern China

44 (Fig. 2).

45 This biomass burning has both local and regional scale air quality impacts, with emissions of particulate matter (PM)

46 of particular concern (Bond et al., 2013). The East Asian monsoon system that influences much of mainland China

47 results in prevailing north-westerly to south-easterly atmospheric transport during winter, which is reversed in the

48 summer months. Under these influences, the smoke from agricultural residue fires in Eastern China often affects

49 "mega-cities" like Beijing and Shanghai (Chan & Yao, 2008; Cheng et al., 2013; Du et al., 2011; Li et al., 2010).

50 Modelling studies show that these agricultural emissions can drive intense regional air pollution episodes; Huang et

51 al. (2012) suggest that $PM_{10}$ concentrations in some cities could reach 600 µg m$^{-3}$ during such episodes, a level 6×

52 higher than the WHO 24h-mean $PM_{10}$ air quality guideline for human health (WHO, 2005).

53 Agricultural burning in eastern China accounts for a significant part of China's total biomass burning emissions

54 (Streets et al., 2003; Chen et al., 2017), however the specific contribution of crop residue burning to air quality

55 exceedances in China remains uncertain, partly because there is considerable doubt as to the amount of dry matter

56 burned (DMB) in crop residue fires. For example, this leads to a ~450 % range in total crop residue burning black

57 carbon emissions in Asia between different emissions inventories (Streets et al., 2003), while emissions estimates of

58 gaseous species are similarly varied.

59 A major source of this uncertainty stems from the hitherto relatively poor ability of earth observation (EO) satellite

60 instruments to adequately detect biomass burning activity in many agricultural areas due to the small size of the fires

61 usually found in these areas. Many agricultural fields in eastern China are typically only around 700 m$^2$ in area (NBSC,

62 2012), and fires ignited to burn across the stubble left in the place after harvest are therefore hard to detect with

63 moderate spatial resolution burned area (BA) mapping from sensors such as MODIS (Moderate Resolution Imaging

64 Spectroradiometer), and are made even more elusive by the common farming practice of pilling up residues into an

65 even smaller area before igniting them (Zhang et al., 2017; 2018). As most BA mapping methods require ~ > 20 % of

66 a pixel to be burned in order for it to be classified as 'fire affected' (Giglio et al., 2006; 2009), BA-based emissions

67 inventories such as GFED (Global Fire Emissions Database) tend to significantly underestimate fire activity in areas

68 such as eastern China (Zhang et al., 2018).

69 Infrared based Active fire (AF) based detection techniques can discriminate fires covering only 0.01-0.1 % of a pixel

70 area (Wooster et al., 2005; Schroeder et al., 2014), and as such should in theory be able to capture far more fire activity

71 in agricultural areas than BA based methods. Nevertheless, due to the extremely small size of agricultural fires in

72 eastern China, a large proportion of fire activity remains undetected by AF detection algorithms applied to 'moderate'

73 spatial resolution imagery (from sensors such as MODIS). This limitation is a key source of uncertainty within the

74 FRP approach, and indeed in fact can lead to biased (underestimated) FRP totals caused by the non-detection of the

75 lower FRP component of a regions fire regime (e.g. Roberts et al., 2015). Higher spatial resolution polar-orbiting

76 sensors such as VIIRS (Visible Infrared Imaging Radiometer Suite) can provide the ability to identify an increased

77 number of AFs having lower FRP values, particularly when used with algorithms optimised for small fire detection

78 (Zhang et al., 2017) (Fig. 2), but they still only capture fires burning in clear skies at the time of the satellite overpass

79 (Giglio et al., 2003; 2006). This limitation is also a considerable source of uncertainty, and a hinderance given the

80 sometimes short duration of active burning (especially of  agricultural fires) and the typical polar orbiting imaging

81 frequency of only a few times per day. To cope with this issue, FRP-based emissions inventories such as GFAS based

82 upon AF methods are generally required to make assumptions or exploit additional data on the timing and relative

83 diurnal variability of fire activity occurring between polar orbiting overpasses in order to estimate, for example, total

84 daily Fire Radiative Energy (FRE) (Kaiser et al., 2012; Xu et al., 2017; Zhang et al., 2017). Here we provide this

85 additional information by exploiting new fire diurnal cycle information taken from the geostationary satellite

86 Himawari-8, combining it with twice daily FRP information provided by the 'small fire optimised' VIIRS-IM product

87 of Zhang et al. (2017) to produce a unique high spatio-temporal resolution agricultural fire dataset (referred to hereafter

88 as the VIIRS-IM/Him dataset) for eastern China based on FRE totals. This new inventory is designed to reduce bias

89 and uncertainty caused by use of one FRP data type alone, and to account for small fires burning even for short periods

90 and often well below the MODIS AF and BA detection limit. The fuel for these fires is waste straw and other

91 agricultural residues, and we use a crop rotation map to classify the type of agricultural residue being burned at each

92 observed location and time. It is then used to select the most appropriate smoke emissions factor for calculating the

93 final fire emissions totals from FRE derived estimates of dry matter burned (DMB).

94

## 2. DATASETS

2.1 Polar Orbiting VIIRS-IM FRP Product

The Visible Infrared Imaging Radiometer Suite (VIIRS) instrument is currently flown aboard the polar orbiting Suomi NPP (since 2011) and NOAA-20 (since 2017) satellites and expands upon the capabilities of the AVHRR and MODIS instruments for environmental monitoring (Zhou et al., 2019). VIIRS has 22 channels spanning the visible to the longwave infrared, a 3000 km swath width, and nadir pixel resolution ranging between 375 m and 750 m (Goldberg et al., 2013). Furthermore, a 'pixel aggregation' scheme is applied to VIIRS which limits pixel area increase with scan angle to a maximum of $4\times$ compared to MODIS' $10\times$ (Wolfe et al., 2013).

With a necessary emphasis on the detection of small fires typical of agricultural regions, our work focuses on generating a gridded daily biomass burning fuel consumption product that estimates DMB and emissions from the VIIRS-IM AF Detection and FRP product developed and optimised for eastern China by Zhang et al. (2017), using data from the instrument aboard the Suomi NPP satellite with a mean local daytime overpass time of 13:30 in the ascending node, and a mean local nighttime overpass time of 01:30 in the descending node (Wolfe et al., 2013). Fig. 2 shows an example of the VIIRS-IM FRP product, generated from the two observations per day provided by Suomi NPP VIIRS. This FRP product blends the advantages of the 'small fire' sensitivity of the VIIRS 375 m I-Band, with the ability to retrieve fire radiative power (FRP) over larger fires using the 750 m M-Band observations. Due to the very small size of agricultural fires in China, and because the VIIRS I-Band pixel area is $10\times$ smaller than the pixel area of MODIS, far more fires can be detected in eastern china using the VIIRS-IM AF product of Zhang et al. (2017) than can be identified in near simultaneous MODIS data, and on average across eastern China retrieves FRP totals around $4\times$ higher (Zhang *et al.*, 2017).

2.2 Geostationary Himawari FRP Product

To convert the twice-daily VIIRS-IM FRP product to daily-integrated FRE, information on the fire diurnal cycle is required (Ellicott et al., 2009; Freeborn et al., 2008; Roberts et al., 2009). We obtained this from 10-min temporal resolution observations from the geostationary Himawari-8 satellite, whose data have recently been used to derive AF detections and FRP metrics across Asia by Xu et al. (2017). Himawari cannot be used in isolation to directly estimate daily FRE for each of the 4-years of the study, because (i) Himawari data are only available from early 2015 onwards, and (ii) Himawari's relatively coarse pixel size (2 km at the sub-satellite point) means that it omits even more of the agricultural fires than does MODIS (as illustrated by Xu et al., 2017 and in Fig.3). However, where agricultural fires are concentrated in sufficient density, observations by Himawari do enable their detection and these data can be used to map the changing FRP of these fires over the day for derivation of the fire diurnal cycle.

2.3 Crop Rotation Map

128    The predominant agricultural residues burned across eastern China are wheat, corn and rice straw (Huang et al., 2012).

129    To classify the likely residue type of each detected fire, a crop rotation map (Fig. S1) was generated from the

130    MIRCA2000 0.08º global monthly crop area dataset (Portmann *et al.,* 2010), which has a spatial resolution equivalent

131    to 9.2 km × 9.2 km at the equator. These data were used to assign fire activity to a particular crop residue type, which

132    determined the appropriate agricultural biomass burning emission factors to apply (see Section 3.3).

133

134    2.4 Land Cover Data

135    We use the GlobeLand30 land cover product (Chen et al, 2015) to classify land cover/use for our study area in Eastern

136    China. GlobeLand30 provides 30m spatial resolution land cover data for a baseline year of 2010 derived primarily

137    from Landsat (TM5 & ETM +) and China Environmental Disaster Alleviation Satellite (HJ-1) imagers. Fig. 1 shows

138    the spatial distribution of the agricultural land ratio (regridded to 0.01 degree spatial resolution) calculated use this

139    dataset in eastern China.

140

141    2.5 GFED & GFAS Emissions Inventory Data

142    The results from the combined VIIRS-IM and Himawari FRP based emissions (VIIRS-IM/Him) dataset were

143    compared to two state-of-the-art global fire emission databases, the Global Fire Emissions Database (GFED) and the

144    Global Fire Assimilation System (GFAS). GFED was built to combine remotely sensed data on BA with fuel loads

145    from the CASA biogeochemical model of vegetation growth, producing monthly, spatially explicit pyrogenic fuel

146    consumption, carbon, GHG and air pollution emission estimates at 0.25º grid cell resolution globally (Van der Werf

147    et al., 2010; Giglio et al., 2013). The most recent version (GFED4.1s) includes a "small fire boost" based on AF

148    detections, in an attempt to counteract the inability of the MODIS BA product to detect many agricultural fires

149    (Randerson et al., 2012; Van der Werf et al., 2017). Due to this 'boost' GFED4.1s shows higher values of dry matter

150    burned (DMB) in most eastern China grid cells compared to the 'unboosted' GFED4, and a more extensive fire

151    distribution. However, Zhang et al. (2018) show that the boosting procedure can introduce significant anomalies into

152    the GFED dataset at certain times of year, generated when MODIS' AF detection procedure incorrectly identifies

153    urban features in eastern China as fires.

154    In contrast to GFED, the GFAS fire emissions database is based on AF detections and is integrated into Copernicus

155    Atmosphere Monitoring Service (CAMS) system for near-real-time atmospheric composition monitoring and

156    forecasting. Developed by Kaiser et al. (2012) and based on the FRP method, MODIS supplies the FRP data for the

157    current GFAS v1.2 up to 4 times per day at most latitudes. From these observations, DMB is calculated via a regression

158    against GFED DMB values (Kaiser et al., 2012) and daily emissions of 40 emitted species are then calculated at 0.1º

159    spatial resolution.

160

161    2.6 Crop Yield Based Approach Emissions Inventory Data

162    The traditional method for estimation of agricultural fire emissions is the so-called crop yield based approach (CYBA),

163    and we compare data from such approaches to our new VIIRS-IM/Him methodology. CYBAs typically calculate the

164    amount of crop residue burned in a region using a combination of crop production statistics and related additional

165    parameters using following equation:

166    $DMB = \sum_{i=1}^{n} P_i R_i B_i C$ (1)

167    Where $i$ stands for each of $n$ different crops; $DMB$ is total dry matter burned (kg) in the region; $P_i$ is the regional

168    production of crop $i$ (kg), and is usually derived from annual agricultural statics reports; $R_i$ is the dry matter production-

169    to-residue ratio (unitless), which depends on the crop type $i$; $B_i$ is the proportion of residue burned in the field for crop

170    type $i$ in the region under study (i.e. the 'burning ratio'; 0-1, unitless); and $C$ is crop combustion completeness (0-1,

171    unitless, Huang *et al.,* 2012). DMB is then multiplied by appropriate particulate/gaseous emission factors in order to

172    estimate the total emissions from agricultural burning.

173    Certain of the parameters of Eqn. 1 are not so easily determined. For example, the burning ratio ($B_i$) is often based on

174    questionnaires or investigations on the use of crop residues conducted with farmers (Gao *et al.,* 2002; Wang and Zhang,

175    2008). Because of strong variations in socio-economic development across the huge expanse of mainland China, large

176    differences in the estimates of $B_i$ exist (Jiang *et al.,* 2012; Liu *et al.,* 2008; Yamaji *et al.,* 2010). $B_i$ may also change

177    considerably from year to year since it is strongly impacted by the level of local economic development, the

178    availability of alternative uses for crop residues in the region, and the regional governance of fire prohibition (Chen

179    *et al.,* 2017). Moreover, considering the official prohibition of open air burning, the reliability of data based on surveys

180    that ask farmer how much residue they burn is questionable. Despite this, most studies that include estimation of

181    agricultural fire emissions in Eastern China have relied on the CYBA (e.g. Cao *et al.,* 2006; He *et al.,* 2011; Huang *et

182    al.,* 2012; Li *et al.,* 2009; Qin and Xie, 2011; Yan *et al.,* 2006; Zhao *et al.,* 2015).

183

184    **3. METHODOLOGY**

185    3.1 Data Gridding and Cloud Cover Adjustment

186    The VIIRS-IM FRP product data (in MW), originally derived at the pixel scale, were aggregated to 0.1° resolution for

187    this analysis. Unlike the daily average MODIS FRP calculation of GFAS, which weights individually contributing

188    MODIS FRP observations by their view zenith angle to downgrade the importance of far off-nadir measurements

189    (Kaiser *et al.,* 2012), no such weighting was applied to the VIIRS-IM FRP data since they have already shown very

190    limited view zenith angle dependence as a result of the VIIRS' pixel-averaging procedure (Zhang et al., 2017). For

191    each VIIRS overpass, the total observed FRP present in each 0.1° grid cell $j$ (i.e. FRP$_j$) was calculated from the

192    cumulative FRP of all native resolution AF pixels $i$ within the grid cell:

193    $FRP_j = \sum_{i \in j} FRP_i$ (2)

194    Total observed agricultural area ($A$, excluding cloud covered area) within each 0.1° grid cell was calculated similarly

195    using the GlobeLand30 30m landcover map:

196    $A_j = \sum_{i \in j} A_i$                                           (3)

197    The VIIRS-IM product is only affected to a limited degree by smoke because of the relative transparency of smoke

198    plumes at Mid-Wave Infrared (MWIR) wavelengths due to the dominant particle size being smaller than the

199    wavelengths of the VIIRS MWIR channel (Zhang et al., 2017). However, the product cannot provide information in

200    cloud covered areas, and so an adjustment is required to take into account actively burning fires hidden from view by

201    clouds. Following Streets *et al.* (2003) we assume that for partially cloud covered grid cells, the AF and FRP

202    distribution under cloud is the same as under the clear sky areas, as is also assumed in GFAS (Kaiser *et al.*, 2012).

203    Subsequently, the gridded and cloud-adjusted FRP areal density ($\rho_j$, MW.km$^{-2}$) is calculated using:

204    $\rho_j = \dfrac{FRP_j}{A_j}$                                          (4)

205    Cloud cover (CC) fractions in some grid cells occasionally reach 0.5 (50%), but most are zero. After the cloud cover

206    adjustment, the mean FRP areal density across the study area increased by 11.5%, so the overall effect of the CC

207    adjustment is relatively minor.

208    3.2 Diurnal Cycle and Daily FRE Generation

209    Hourly averages of the 10-minute FRP data from the Himawari-8 FRP product of Xu *et al.* (2017) were gridded to the

210    same 0.1° grid cell resolution as the VIIRS-IM dataset. For each grid cell and calendar day, hourly FRP data were

211    normalised in order to minimise the impact of day-to-day variations in fire activity:

212    $\widetilde{FRP_{j,d}^{h}} = \dfrac{FRP_{j,d}^{h} - \min(FRP_{j,d})}{\max(FRP_{j,d}) - \min(FRP_{j,d})}$                     (5)

213    Where $\widetilde{FRP_{j,d}^{h}}$ is the normalised Himawari-8 FRP for hour $h$ on day $d$ for grid cell $j$; $FRP_{j,d}^{h}$ is the averaged Himawari-

214    8 FRP (MW) for hour $h$ on day $d$ for grid cell $j$; $\max(FRP_{j,d})$ and $\min(FRP_{j,d})$ are respectively the maximum and

215    minimum hourly Himawari-8 FRP (MW) observed on day $d$ for grid cell $j$. Note that $h$ is in local time (UTC/GMT +

216    8 hours) and the diurnal cycle runs from 0 to 23 hours.

217    $\widetilde{FRP_{j,d}^{h}}$ data for 2015 were used to produce two normalised 'seasonal' diurnal fire cycles for the eastern China study

218    area: a 'summer' diurnal cycle, constructed from May-June data, and an 'autumn' diurnal cycle, constructed from

219    Sept-Oct data. Both normalised seasonal diurnal cycles were calculated using a weighted mean so that days and grid

220    cells with high fire activity had the greatest influence on the cycle:

221    $$FRP^h = \frac{\sum_d \sum_j \left( \widetilde{FRP_{j,d}^{h}} \times FRP_{j,d}^{h} \right)}{\sum_d \sum_j \left( FRP_{j,d}^{h} \right)}$$             (7)

222

223 Where $FRP^h$ is the normalised FRP for hour $h$ for the entire study area and fire season (summer or autumn). Fig. 4

224 shows the resulting weighted mean fire diurnal cycle for the summer season for Eastern China. This diurnal cycle is

225 bi-modal: a primary peak occurs around 13:00 local time that extends from around 08:00 to 18:00 (daytime) and a

226 second much smaller peak occurs around 21:00 local time (with a magnitude of only $\sim$ 20% of the normalised FRP

227 value of the first peak).

228 We blended information from the Himawari FRP diurnal cycle with the instantaneous twice-daily VIIRS-IM FRP

229 areal density ($\rho_j$, MW.km$^{-2}$) data, using an approach based on Andela et al. (2015) to create the VIIRS-IM/Him dataset.

230 Here we represent the diurnal fire cycle as a gaussian function parameterised using the Himawari FRP diurnal cycle,

231 superimposed on a fixed baseline. For a given grid cell $j$, at instantaneous time $t$, VIIRS-IM/Him FRP areal density is

232 calculated by:

233

234
$$\rho_{VIIRS-Him_{j,t}} = \rho_{VIIRS_{night,j}} + \mu\left(\rho_{VIIRS_{day,j}} - \rho_{VIIRS_{night,j}}\right) e^{-\frac{\left(t - t_{Himpeak}\right)^2}{2\sigma^2}} \tag{8}$$

235

236 Where $\rho_{VIIRS-Him_{j,t}}$ is the instantaneous VIIRS-IM/Him FRP areal density (MW.km$^{-2}$) for grid cell $j$ at time $t$;

237 $\rho_{VIIRS_{night,j}}$ is the night-time (~01:00 LST) VIIRS-IM FRP areal density value (MW.km$^{-2}$) for grid cell $j$; $\rho_{VIIRS_{day,j}}$

238 is the day time (~13:00 LST) VIIRS-IM FRP areal density value (MW.km$^{-2}$) for grid cell $j$; $\mu$ is an adjustment factor

239 used to account for the difference between the VIIRS daytime overpass time and the peak time of the weighted mean

240 fire diurnal cycle (Eqn. 9); $t_{Himpeak}$ is the time of day at which the seasonal Himawari FRP diurnal cycle peaks; $\sigma$ is the

241 standard deviation of the main peak of the Himawari FRP diurnal cycle, calculated by fitting a gaussian function

242 (using non-linear least squares) to the seasonal Himawari FRP diurnal cycles. The summer diurnal cycle $\sigma$ value

243 (2.39±0.053) was applied during the April-August period, and the autumn diurnal cycle $\sigma$ value (1.63±0.041) was

244 applied during the September-March period.

245 The adjustment factor $\mu$ is used to account for the fact that the VIIRS daytime overpass time is unlikely to coincide

246 with the peak of the fire diurnal cycle:

247

248
$$\mu = e^{\frac{\left(t_{VIIRS_{day,j}} - t_{Himpeak}\right)^2}{2\sigma^2}} \tag{9}$$

249

250 Where $t_{VIIRS_{day,j}}$ is the local time of the VIIRS-IM FRP observation for grid cell $j$.

251 Daily FRE was then estimated for each grid cell j and calendar day by integrating the instantaneous VIIRS-IM/Him

252 FRP data using Eqn. 8.

253

254     3.3 Conversion to Dry Matter Burned (DMB) and Smoke Emissions

255     To convert the estimated FRE areal density to fuel consumption/DMB, we multiplied FRE by the 0.368 ($\pm$0.015)

256     kg.MJ$^{-1}$ factor derived by Wooster *et al*. (2005) from a series of outdoor experimental straw fires, that were very

257     similar to the Chinese agricultural residue fires used herein (Zhang et al., 2015). To convert the resultant DMB into

258     smoke emissions, we used the emission factors of wheat and rice derived from *in situ* measurements in agricultural

259     areas by Zhang et al. (2015) (Table 1). Corn residue was not a fuel type measured during those experiments, and so

260     for this fuel type (which was only 16-22% of the total agricultural fuel consumption) we used the emissions factors

261     for agricultural corn fires from Andreae and Merlet (2001), as is used in GFAS (Kaiser *et al.,* 2012) (Table 1). Together

262     with the crop rotation map (see Section 2.3 and Fig. S1) the EFs from Table 1 enabled us to select the appropriate

263     emissions factor for use at a particular location and time of year.

264     Furthermore, a winter burning season was discovered during November and December (see details in Section 5.1)

265     when no cultivation crop is shown in the MIRCA2000 data in the study region. Analysis in this study shows that

266     winter fires are likely to result from the combustion of stored residues from the autumn harvest season, therefore all

267     fire activity in winter was assigned to crop types (and therefore emission factors) using the crop rotation map from the

268     previous closest month (October) (Fig. S1). This methodological change is accounted for in the data presented in Fig.

269     5.

270

271     **4. BIOMASS BURNING AND EMISSIONS RESULTS**

272     4.1 Temporal and Spatial Distribution of FRE In Eastern China

273     Fig. 5 shows the time series of daily mean FRE areal density in eastern China from February 2012 to December 2015,

274     reported at 0.1$^{o}$ grid cell resolution, and broken down into three main crop residue types. A strong seasonal variation

275     is seen, with peak activity in summer (May-June) associated with wheat residue burning and a smaller secondary peak

276     in activity occurring in autumn (Sept-Oct) associated with corn and rice residue burning. In fact, the secondary peak

277     is a combination of several fluctuations lasting from October until December, further discussed in Section 5.1. Over

278     the whole 4-year period, wheat crop residues contributed 65% of the total FRE, rice residues 18%, and corn residues

279     17%.

280     A distinct spatial pattern showing two main burning seasons can also been seen when FRE areal density is mapped

281     (Fig. 6). During the summer burning season (May-June), most fires are located between 32$^{o}$ N - 36$^{o}$ N, extending from

282     112$^{o}$ E - 120$^{o}$ E near the coast. In the autumn season (Sept-Oct), less fire activity occurs than in the summer fire season

283     and it is more evenly distributed across the entire study area, though there is still a focus of fire activity between 32 -

284     34$^{o}$ N and 112 - 119$^{o}$ E. Moreover, in the southwest of the study area (29 - 32$^{o}$ N and 112 - 114$^{o}$ E) we see a region

285     that only appears to undergo substantial burning in the autumn. This is located in the centre of Hubei Province, which

286     contributes around 12% of the total rice yield of the whole of China (NBSC, 2015). This area contributes to between

287     10 and 18 % (year dependant) of the total autumn burning season FRE.

288

289     4.2 DMB Comparisons to GFAS and GFED

290     The outputs generated by our combined VIIRS and Himawari processing chain were compared to those of GFAS and

291     GFED4.1s (Fig. 7). Dry matter burned (DMB) was used as the common comparison metric, as this removes differences

292     arising from the use of different emissions factors within the inventories. Overall, the VIIRS-IM/Him DMB estimates

293     are around 2× to 5× higher than those reported for corresponding months by GFAS and GFED 4.1s. As detailed in

294     Zhang et al. (2017) and discussed in Section 2, VIIRS has the ability to detect far smaller (and lower FRP) fires than

295     MODIS, due to its far smaller pixel size and the fact that the I-band observations also retain their pixel area more

296     effectively across the swath. Ultimately, this difference results in far higher DMB being obtained by the VIIRS-

297     IM/Him inventory compared to the MODIS based GFAS and GFED inventories.

298     During the summer months of May-June, all three inventories (GFAS, GFED and VIIRS-IM/Himawari) show a clear

299     peak in DMB, but GFAS and VIIRS-IM/Him show a much sharper peak in June, while GFED's summer burning

300     season extends one month earlier (May) and later (July). This extended summer fire season reported by GFED is likely

301     the result false fire reporting, discussed at length in Zhang et al (2018). VIIRS-IM/Him shows a June DMB peak

302     ranging from 3.30 to 11.2 Tg, 2× higher than GFED4.1s (1.89 - 5.34 Tg) and GFAS (2.00 to 4.30 Tg). It should be

303     remembered that the conversion of daily average FRP to DMB in GFAS is derived via a calibration to GFED4.1s

304     (Kaiser *et al.*, 2012), so these two emissions databases understandably report similar monthly DMB totals.

305     For the autumn (Sept-Oct) burning season, the peaks in the GFAS and GFED inventories are much less pronounced

306     than the summer burning season peaks (Fig. 7). DMB in October ranges from 0.57 - 1.74 Tg for GFED, significantly

307     higher than the 0.31 - 0.61 Tg reported by GFAS, but far lower than the 1.62 - 3.05 Tg of the VIIRS-IM/Him inventory.

308     The VIIRS-IM/Him derived DMB estimates for eastern China are thus 2 to 3× higher than GFED4.1s and 5× higher

309     than GFAS; these represent larger differences than exist for the earlier summer burning season. This indicates that

310     agricultural fires burning during the autumn fire season may be on average smaller and/or more isolated from other

311     fires than they are in the summer burning season, and thus are even more likely to be missed by the MODIS AF

312     detection product (Giglio *et al.,* 2006) and/or the MODIS BA product (Giglio *et al.,* 2013) than they are during other

313     more intense burning periods.

314

315     4.3 Agricultural Fire Emissions Intercomparison

316     This section presents a comparison of the total annual agricultural fire emissions calculated using the VIIRS-IM/Him

317     method with other inventories of Chinese agricultural fire emissions in the literature, and against emissions totals from

318     other sectors to gain a better understanding of the relative importance of agricultural fire emissions. To compare with

319   other reported agricultural fire emission inventories for China, the DMB estimates produced herein were converted to
320   fire emissions estimates using the emissions factors and methods described in Section 3.3; these results are summarised
321   in Fig. 8 and Table 2.

322   From Fig. 8, it is clear that wheat residue burning is the primary agricultural emission source, accounting for over 50%
323   of the total emissions released each year (specifically 55-69% of $PM_{2.5}$, 71-81% of BC, 66-77% of $CO_2$, and 69-80%
324   of CO). Fig. 8 also indicates a considerable reduction in emissions in 2015 compared to previous years, largely
325   attributable to a reduction in the amount of wheat residue burnt. For example, total $PM_{2.5}$ emissions from agricultural
326   residue burning in eastern China for 2012-14 cover a relatively narrow range of 107 - 130 Gg (Fig. 8 & Table 2), but
327   decrease to $67 \pm 24$ Gg in 2015 due to an almost halving of DMB (Fig. 7); similar patterns are observed for BC, $CO_2$,
328   and CO (Fig.8).

329   From Table 2, it is apparent that emissions totals calculated using the VIIRS-IM/Him approach are consistently higher
330   than those reported by GFAS by factor of 1.2-4.2 (species/year dependent). Similarly, VIIRS-IM/Him emissions totals
331   for $CO_2$ and PM2.5 are greater than those reported by GFED by a factor of 1.1-1.7. In both cases, this can be explained
332   by the tendency of MODIS to miss activity from small fires compared to VIIRS. VIIRS-IM/Him emissions for CO
333   and BC in 2015 are lower than those reported for GFED, which can be attributed to differences in the emissions factors
334   used between the approaches.

335   Emissions totals calculated using the VIIRS-IM/Him approach are smaller than those estimated by CYBA studies for
336   the East China/North China Plain regions (Zhang et al., 2008; Huang et al., 2012; Qiu et al., 2016) by a factor of 2-5.
337   It is possible that the much higher totals estimated from the CYBA based studies maybe due to the use of very high
338   residue burning ratios ($B_i$ in Eq. 1) for corn and rice in particular. This finding is discussed further in Section 5.

339   Liu *et al.,* (2015) estimated total emissions in the North China Plain region (a similar area to the study area used in
340   this paper) using MODIS FRP-based calculations, and assumed a modified Gaussian function for the diurnal cycle to
341   generate the daily FRE estimates from which emissions were then derived. These estimates are much closer in
342   magnitude to the equivalent estimates calculated using the VIIRS-IM/Him method than those from the CYBA studies,
343   however 2013 & 2014 estimates by Liu et al. are consistently lower (by a factor of 0.3-0.9); again, we attribute this
344   difference to the fact that MODIS based methods capture less fire activity than our VIIRS-IM/Him approach.
345   Interestingly, Liu *et al.* (2015) estimated far higher emission totals for 2012 compared to 2013 & 2014 and report
346   greater total CO and BC emissions than we do. For example, annual $CO_2$ emissions in 2012 (26,000 Gg) are $> 2\times$ their
347   reported total emissions for 2013 (9800 Gg) and 2014 (13,000 Gg). However, Liu *et al.*'s processing approach did not
348   provide any adjustment for the impact of the MODIS 'bow-tie' scan geometry effect, which leads to duplicated AF
349   detections and this FRP towards the edge of the MODIS swath, and which was highlighted as significant issue for
350   FRP quantification by Freeborn *et al.* (2008) and Zhang et al. (2017). This is a particular problem in MODIS data
351   from the year 2012, where large amount of duplicated observations have been found towards edge of swath (Fig. S2).
352   This problem has been addressed in GFAS using a scan-angle dependent weighing factor for the MODIS FRP data

353    (Kaiser *et al.,* 2012), as described in Section 2.5, and GFAS' $CO_2$ emissions from 2012 are only 24% and 10% higher

354    than from 2013 and 2014 respectively, a much more modest increase compared to that reported in Liu *et al.* (2015).

355    Fig. 9 presents a comparison of agricultural emissions calculated using the VIIRS-IM/Him method with emissions

356    from non-biomass burning sources produced by Li et al. (2014) for a sub-area of eastern China (32-36º N, 112-122º

357    E) for the year 2013. We note that crop burning emissions are of relatively little significance when considered on an

358    annual basis; for all four species ($CO_2$, CO, $PM_{2.5}$, BC), contributions from agricultural residue burning range between

359    0.56% and 2.0% of total annual emissions, with the majority of emissions resulting from industry and residential

360    sources. However, in June when agricultural burning and emissions are at a maximum, residue burning contributes

361    8.1%, 18%, 22% and 20% of total monthly emissions for $CO_2$, CO, $PM_{2.5}$ and BC respectively, highlighting the strong

362    seasonal impact agricultural burning can have on the emission of species that affect both climate and air quality.

363

364    **5. ANALYSIS AND DISCUSSION**

365    5.1 Importance of Wheat Residue Burning

366    Findings in Section 4 (Fig. 5 & 8) indicate that a larger proportion of wheat residue than corn or rice residue is burnt,

367    for several reasons. First, the yields of these three crop types in Eastern China are relatively similar - in 2015 for

368    example, wheat yield was 10% lower than rice yield, and only 20% higher than corn (Table S1; NBSC, 2015). Second,

369    the dry matter production-to-residue ratio ($R_i$ in Eqn. 1) of wheat is not higher than that of rice or corn (Table S2;

370    Wang and Zhang, 2008). Third, with the exception of black carbon, the emission factors for wheat residues are broadly

371    similar to or smaller than the corresponding rice and corn emission factors. It is unknown why a greater fraction of

372    wheat residue than corn and rice residue is burnt, however, it is possible that local management practices and/or

373    stakeholder priorities differ depending upon the residue type and time of year at which crops are harvested, ultimately

374    impacting the fate of these residues e.g. residues from certain crops maybe valuable as fertiliser (Huang et al., 2012),

375    animal feed or for domestic/local energy production (Chen et al., 2017; Liu et al., 2008).

376

377    5.2 Discovery of A Winter Burning Season

378    As detailed in Section 4.1, small peaks in our dry matter burned (DMB) time-series are apparent in November-

379    December of each year (grey shaded area shown in Fig. 5). Since no mention of such a winter burning season was

380    found in the literature (e.g. Chen *et al.,* 2017; Huang *et al.,* 2012; Zhang *et al.,* 2008), these winter peaks were initially

381    considered to be erroneous and likely caused by VIIRS AF false alarms that had failed to be excluded by the landcover

382    and/or persistent thermal anomaly masking detailed in Zhang et al., (2017). Furthermore, according to the crop rotation

383    map derived from the MIRCA2000 data (Fig. S1), there is no obvious harvesting of wheat, corn, or rice during the

384    winter in eastern China. However, close examination of the original VIIRS data and the VIIRS-IM FRP product

385    generated from it by Zhang et al., (2017) shows that most of the AF pixels detected in eastern China in winter are in

386    fact located in or very close to areas classified as agricultural land (Fig. S3), and are not located close to industrial

387      areas of the type known to cause false AF detections (Zhang et al., 2017), nor do the AF detections appear multiple

388      times in the same month at the same location, as would be expected if they were false alarms generated by non-fire

389      features. It therefore seems highly probable that these AF detections are actually a consequence of true agricultural

390      burning (Fig. S3-5).

391      The most reasonable explanation for the winter AFs appears to be that some of the crop residues from the Sept-Oct

392      (Autumn) harvest season were left idle for a few months and burned in the winter, rather than immediately. Local

393      newspapers, online media and other information sources were consulted, and were found to support the existence of

394      winter residue burning episodes. One example is a report by Jiangsu Province TV station in 5 December 2013, where

395      a huge crop residue burning episode was reported in Hongze (Jiangsu Province), close to the location shown in Fig.

396      S3. Stills from this TV report show flames, thick smoke and extremely poor visibility resulting from the crop residue

397      burning, described in Chinese language subtitles (Fig. S4). Reports of similar episodes were found in different

398      websites/newspapers from across much of eastern China (e.g. Wang and Zhang, 2016; Za, 2015; Zuo, 2015).

399      Subsequent to this confirmation, an explanation as to why this activity may have occurred outside of the normal

400      burning season was sought. According to Yun Xia, a local governor of the Environmental Department in Hefei

401      (interview conducted by Anhui News; Zuo, 2015), the prohibition on agricultural burning started at beginning of

402      September in that area, and continued up until the 20th November. During this period, the local government strongly

403      enforced its polices aiming to restrict agricultural residue burning, and established almost continuous patrols to

404      identify areas likely to host crop residue fires in order to prevent their ignition. However, without a widespread and

405      cost-effective alternative way to dispose of their crop residues, local farmers may simply have stored the residue

406      material and burned it soon after the end of the prohibition period, when the intensive patrol period had ceased. The

407      end of the prohibition period coincides almost exactly with the time of the new winter burning season identified by

408      our VIIRS-IM/Him dataset (Figs. 5- 7).

409      The winter season is important for biomass burning in this area of China, accounting for between 19 and 36 % (year

410      dependant) of the combined autumn and winter FRE total. Based on the crop rotation map (Fig S1), this fire activity

411      was assigned to the burning of both corn and rice residues, with the contribution of each residue to total FRE (and

412      thus DMB) almost equal (49 % and 51 %, average over all years). This split by residue type is very similar to that

413      observed in the Autumn burning season (corn = 54 %, rice = 46 %, average over all years), despite the observed

414      variation in the spatial distribution of fire between autumn and winter (Fig. 6). In general, winter burning appears to

415      take place closer to provincial capitals than autumn burning does; the reason for this spatial shift in fire is discussed

416      in Section 5.4.

417

418      5.3 Disagreement Between Satellite Derived Emissions and Crop Yield Based Approaches

419      In Section 4.3, it was noted that annual emissions totals calculated using crop yield based approaches (CYBAs) are

420      greater than those calculated using the VIIRS-IM/Him method by a factor of 2-3, depending on species. We believe

421      that this discrepancy relates to the 'burning ratio' (BR) used in CYBA to produce emissions estimates. The burning

422  ratio is the ratio of crop residue burned in the field compared to the total amount of residue produced by harvesting,

423  and is a key parameter in bottom up CYBAs (see Eqn. 1, and Chen *et al.,* 2017; Gao *et al.,* 2002; Huang *et al.,* 2012;

424  Li *et al.,* 2016). Streets *et al.* (2003) used a uniform BR of 17 % derived from 1970's data, however more recent

425  studies often make use of regionally varying fractions. We identified three sources of regionally varying burning ratios

426  that are widely used in the CYBA literature:

427  i)  Wang and Zhang (2008), divided all provinces in China into six zones according to their geographical

428  distribution. A questionnaire-based survey conducted amongst farmers within these regions was used to

429  elucidate the level of burning activity, and using the responses it was determined that burning ratios for

430  the different categories ranged from 11% to 33%. Outputs were applied and referenced in a series of fire

431  emission studies (He *et al.,* 2011, Qin and Xie 2011, Zhang *et al.,* 2016).

432  ii)  Gao *et al.* (2002) derived a set of province-dependent burning ratios adopted from a large-scale

433  investigation of crop residue use across different Chinese provinces. These ratios have been used and

434  referenced in Huang *et al*. (2012), Yan *et al*. (2006), Zhang *et al*. (2008), and are shown in Fig. 10.

435  iii)  A derived value based on farmers' income levels, based on the fact that Cao *et al.,* (2006) found a positive

436  linear correlation between the income of farmers and burning ratio (r = 0.81). This relationship has been

437  applied within several fire emission studies (Sun *et al.,* 2016, Zhao *et al.,* 2015) and will be examined in

438  Section 5.4.

439  Using crop yield information and the DMB data derived from the VIIRS-IM/Him processing performed herein, it is

440  straight forward to reverse the CYBA methodology to calculate the burning ratio for each crop type. This procedure

441  can help confirm whether the outputs derived herein are comparable with those of the existing literature, as well as

442  enabling the advantages offered by the remote sensing time series to be fully exploited. The burning ratios ($B_{ij}$) for

443  each province *i* and crop type *j* are calculated from:

444  $B_{ij} = \frac{DMB_{ij}}{P_{ij}R_i C}$ (10)

445  Where $DMB_{ij}$ is the estimated VIIRS DMB (g/m$^2$) for province *j* and crop *i*; $P_{ij}$ is the yield of crop *i* for province *j* (kg);

446  $R_i$ is the dry matter production-to-residue ratio for crop *i* (unitless) and *C* is crop combustion completeness (proportion,

447  0-1). The province level crop yield $P_{ij}$ is derived from annually published statistical reports, and are presented in Table

448  S1. $R_i$ and *C* are from Huang et al., (2012); and are presented in Table S2.

449  The crop and province dependent burning ratios calculated from the VIIRS-IM/Him data are shown in Fig. 10,

450  alongside the burning ratios from Gao *et al*. (2002). Fig. 10 indicates that there is considerable variation in burning

451  ratios between individual provinces, and that VIIRS-IM/Him wheat burning ratios for are clearly much higher than

452  rice/corn burning ratios. When averaged over the entire Eastern China study area, yearly mean burning ratios from

453  our results for wheat are highest (7.8 - 12%), followed by corn (1.7 - 2.3%), then rice (0.9 - 2.0%). Equivalent mean

454  burning ratios calculated using data from Gao *et al*. (2002) are 9.8 %, 5.9 % and 8.5 %, respectively. While VIIRS-

455  IM/Him wheat residue burning ratios are in reasonable agreement with those used in the various CYBA studies, our

456   rice and corn burning ratios are much lower; this appears to explain why total annual emissions from the VIIRS-

457   IM/Him approach are much lower than the total emissions obtained from the CYBA studies.

458   Fig. 10 also indicates that burning ratios are not only influenced by crop type and province, but also vary considerably

459   from year to year. For example, in 2012, satellite derived wheat burning ratios for the important agricultural provinces

460   of Anhui (30%), Shandong (11%), Jiangsu (24%) and Henan (11%) are not dissimilar to corresponding ratios (20%,

461   8%, 10%, 7% respectively) from Gao *et al.,* (2002). However, during 2015, values derived in this study are much

462   lower (Anhui = 6 %; Shandong = 4 %; Jiangsu = 4 %; Henan = 6 %). This interannual variation may be linked with

463   changing local farming activity and prohibition policies (Chen *et al.,* 2017, Li *et al.,* 2016, Yang *et al.,* 2008).

464   We believe that the disagreement between the burning ratios derived here and those used in CYBA derived studies

465   indicate that emissions inventories derived using traditional CYBAs may be overestimating agricultural burning

466   emissions, for two main reasons: (1) there appears to be considerable uncertainty and subjectivity associated with the

467   methods used to estimating burning ratios used in CYBA studies, and (2) many burning ratios used in CYBA studies

468   are taken from relatively old (>5-10 years) sources of data. For example, Street *et al.* (2003) use data from 1970's,

469   while most recent researchers use burning ratios from Wang and Zhang (2008) and Gao *et al.* (2002) as listed above

470   in this section.

471   As shown by this analysis, burning ratios appear to be subject to high spatial and interannual variability due to rapidly

472   changing agricultural policies and decision making that influences the fate of crop residues. As such, in order to ensure

473   reliable emissions estimates, we suggest that future agricultural emission studies and inventories that are based upon

474   CYBAs should endeavour to use burning ratios derived from data (1) with high granularity, and (2) that was collected

475   in the corresponding inventory year.

476

477   5.4 Influence of Social Factors on Agricultural Burning

478   As highlighted in Section 5.2, some studies assume a positive relationship between burning ratio and the mean local

479   income of farmers (Cao *et al.,* 2006; Qin and Xie, 2011). The explanation for this is that higher income areas have

480   better access to electricity and other energy sources, and thus have less need to utilise crop residues for heating and

481   cooking – leading to higher ratios of open burning at these locations. However, this is not what we observe in from

482   analyses carried out for this study. In Fig. 11a, minimal correlation was found between GDP and burning ratio, and

483   there is some suggestion of an inverse relationship between these variables (y=-89x+9542, $r^2$=0.13). When directly

484   comparing GDP with DMB,  as Fig. 12 demonstrates, the provinces with the highest average annual DMB per $m^2$

485   (Anhui and Henan; 46 and 27 $g.m^{-2}.yr^{-1}$ respectively) have lower GDP values (US\$ 5,580 and 5,335 per capita) than

486   provinces with lower annual DMB densities (e.g. Shandong and Jiangsu, with 15 and 21 $g.m^{-2}.yr^{-1}$ respectively) but

487   high GDP per capita (USD\$ 9,882 and 13,311 respectively). In fact, across the eastern China study area, our annual

488   total DMB metric was found to be somewhat inversely correlated with GDP per capita ($r^2$ = 0.33; Fig. 11b).

489    We theorise that the observed inverse correlation between GDP and DMB results from the fact that alternative residue

490    disposal methods to biomass burning have a relatively high cost, and can only be afforded by wealthier

491    farmers/provinces. For example, the local government of Jiangsu Province (a relatively wealthy province [\$ 13,311

492    per capita] with only moderate DMB [21 $g.m^{-2}.yr^{-1}$]) released a regulation in 2009 stating that by the end of 2012, over

493    35% of crop residues should been incorporated into the soil after mechanised harvesting. The regulation also indicated

494    that the local government should include a budget for improving the efficiency of agricultural machinery and subsidise

495    farmers who follow this regulation. Furthermore, alternative uses for crop residues are often expensive, and are likely

496    only a viable option in relatively wealthy areas. For example, research on residue burning for power generation shows

497    the government needs to pay at least 20% of the total cost of the operation to keep the power plants running, partly

498    because of the high costs associated with residue collection and transportation from the fields (Li and Hu, 2009).

499    In addition to influencing the quantity of material burned and when it is burned, societal factors also appear influence

500    the spatial pattern of burning within provinces, and at more granular levels such as at the 0.1° grid cell level. The work

501    presented in Section 5.1 suggests that the winter burning season (Nov-Dec) is caused by delayed burning of residues

502    left over from the autumn harvest season, because of prohibition policies related to burning being more robustly

503    enforced earlier in the season. Fig. 6 also showed that the spatial distribution of FRE areal density during winter is

504    different from the normal autumn burning season that occurs in Sep-Oct. Generally, the areas of strongest burning are

505    further from the provincial capital cities (marked by the green stars in Fig. 6) during autumn. For example, fires in

506    Anhui Province are mainly distributed in the north during autumn, whilst fire locations change to the south (closer to

507    the capital city of Hefei) during the delayed winter burns. A similar example can also be seen in Hubei Province,

508    where fires shift from west to east from the autumn to winter burning seasons.

509    To examine this in a more quantitative manner, we calculated the distance from each grid cell shown in Fig. 6 to their

510    provincial capitals. Fig. 13 shows the normalised frequency distribution of the distance from the capital to the top 10%

511    of FRE releasing grid cells in each province, using data from the four burning seasons during the 2012-2015 period.

512    The first and third distance quartiles during the autumn season are 109 km and 214 km respectively, but for the 'lagged'

513    winter burning season, the distribution shifts to far shorter distances (first and third quartiles of 70 km and 153 km

514    respectively). Similarly, the mean distance from provincial capitals also decreased from 165 km in autumn to 124 km

515    in winter. A Kolmogorov–Smirnov (K-S) test was performed to evaluate the difference between the distributions of

516    distance data for the autumn and winter burning seasons, and the resulting high K-S statistic ($0.30, p < 0.001$) indicates

517    that the distribution of distances during the winter months is substantially different to the autumn distance distribution.

518    Similar results were found when we applied the K-S test to each calendar year of data separately (not shown). One

519    possible explanation for this observed difference is that the geographical shift might also be linked with the policies

520    aimed at prohibiting burning, since areas close to capital cities are likely to have more resources for enforcing the

521    prohibition compared to areas more distant from the major urban populations.

522

523

## 6. SUMMARY AND CONCLUSION

We have developed a new state-of-the-art agricultural burning emissions inventory ('VIIRS-IM/Him') for eastern China by combining fire radiative power (FRP) observations from the VIIRS and Himawari-8 sensors for the 2012-2015 period. While several other studies have also used satellite EO data to develop such inventories, they have all relied on MODIS fire products for their source observations. Such inventories include the global GFED and GFAS inventories, several Chinese regional studies (e.g. Huang et al., 2012, Liu et al., 2015). MODIS fire products are known to show very high omission rates in environments dominated by small agricultural fires (Randerson et al., 2012; Zhang et al., 2017, 2018), but the 'small fire optimised' VIIRS-IM product of Zhang et al. (2017) used in this study detects far more of the fire activity across eastern China and on average show FRP totals around 4x higher than those of the MODIS AF products. To convert the twice-daily VIIRS-IM FRP product information to daily time-integrated FRE, we have used new diurnal fire cycle data from Himawari-8, a geostationary satellite positioned over east Asia that can best capture the specific diurnal fire variability of the agricultural burning regions.

Our final VIIRS/Him agricultural fire emissions inventory reports dry matter burned (DMB) totals around 2-5× higher than is reported by GFAS and GFED 4.1s in eastern China for corresponding time periods. Use of a crop rotation map allowed our VIIRS-IM/Him fire and emissions outputs to be disaggregated by individual crop types, and we found wheat residue burning to be the primary agricultural emission source, accounting for over 50% of the total emissions each year for all investigated smoke constituents ($CO_2$, CO, $PM_{2.5}$ and black carbon). A strong seasonal variation in fire activity and emissions is seen, with annual peak activity occurring in summer (May-June) as a result of wheat residue burning, and a smaller secondary activity peak occurring in autumn (Sept-Oct) as a result of corn and rice residue burning. Furthermore, we discovered a new winter (Nov-Dec) agricultural residue burning season. As no crop harvesting occurs during winter, we suspect that this fire activity results from farmers burning previously stored residues from the autumn harvest in winter, after autumn residue burning prohibitions have been lifted. This theory is supported by our observation of statistically distinct spatial burning patterns in the autumn and winter seasons; the majority of autumn burning occurs at a greater distance from provincial capitals than the winter burning does. This may reflect stronger enforcement of autumn residue burning prohibition measures in close proximity to major urban population centres than in rural locations. Farmers in areas with stronger prohibition enforcement (typically closer to urban areas) then burn their agricultural residue in winter.

Detailed comparison to existing inventories showed that our VIIRS-IM/Him annual emissions totals are 1.2-4.7× greater than those reported by GFAS, and 0.5-1.7x those reported by GFED4.1s, with some inter-species variability due to the use of different emissions factors between the inventories. By contrast, the VIIRS-IM/Him inventory shows emissions totals that are on average lower than those from emission inventories derived using crop yield based approaches (CYBA) by a factor of 2-5x. This discrepancy is believed to be primarily due to many CYBAs using outdated and/or inappropriate burning ratios, that consequently leads to CYBAs overestimating the amount of crop residue DMB annually. Back calculated burning ratios from the VIIRS-IM/Him data suggest that burning ratios for rice and corn are much lower than the CYBA literature suggests (approx. 0.9-2.3 % rather than 11-33 %). We also noted considerable inter-provincial and interannual variation in these back calculated burning ratios, for example,

560 wheat burning ratios significantly decrease over our four-year study period. This strongly suggests that high spatial

561 resolution, up-to-date burning ratios should always be used in CYBA for agricultural burning fire emission estimation.

562 Furthermore, several CYBA approaches (e.g. Sun *et al.,* 2016, Zhao *et al.,* 2015) have derived burning ratios from

563 provincial GDP data, assuming a positive relationship between these variables (Cao *et al.,* 2006). However, we found

564 evidence of an opposite (i.e. negative) relationship between provincial GDP and the amount of DMB in agricultural

565 fires, hypothesised to be due to the higher cost of disposal of crop residues by non-biomass burning methods. This

566 suggests that great care needs to be taken when deriving burning ratios for use in future agricultural emissions

567 inventories based upon CYBA methods, and that satellite remote sensing approaches based on EO datasets that

568 adequately detect the presence of agricultural fires are a far better approach to fire emissions estimation in such

569 environments.

570

571

572 **ACKNOWLEDGEMENTS**

573 This work has been supported by the NERC National Centre for Earth Observation (NE/R000115/1) and specifically

574 by NERC Grant NE/M017729/1. The VIIRS SDR and MODIS data were retrieved from CLASS and Reverb, and are

575 courtesy of the NASA EOSDIS LP DAAC and USGS EROS Centre, South Dakota. GFAS data was generated using

576 Copernicus Atmosphere Monitoring Service Information, operated by ECMWF. All data storage and processing were

577 conducted using the UK's JASMIN super-data-cluster system, managed by UK STFC's Centre for Environmental Data

578 Analysis (CEDA).

579

580 **REFERENCES**

581 Andela, N., Kaiser, J.W., Van der Werf, G.R. and Wooster, M.J., 2015. New fire diurnal cycle characterizations to improve fire
582     radiative energy assessments made from MODIS observations. Atmospheric Chemistry and Physics, 15(15), pp.8831-8846.
583 Andreae, M. O. & Merlet, P. 2001. Emission of trace gases and aerosols from biomass burning. Global biogeochemical cycles,
584     15(4), pp 955-966.
585 Bond, T. C., Doherty, S. J., Fahey, D., Forster, P., Berntsen, T., DeAngelo, B., Flanner, M., Ghan, S., Kärcher, B. & Koch, D. 2013.
586     Bounding the role of black carbon in the climate system: A scientific assessment. Journal of Geophysical Research:
587     Atmospheres, 118(11), pp 5380-5552.
588 Cao, G., Zhang, X. & Zheng, F. 2006. Inventory of black carbon and organic carbon emissions from China. Atmospheric
589     Environment, 40(34), pp 6516-6527.
590 Chan, C. K. & Yao, X. 2008. Air pollution in mega cities in China. Atmospheric Environment, 42(1), pp 1-42.
591 Cheng, Y., Engling, G., He, K. B., Duan, F. K., Ma, Y. L., Du, Z. Y., Liu, J. M., Zheng, M. & Weber, R. J. 2013. Biomass burning
592     contribution to Beijing aerosol. Atmos. Chem. Phys., 13(15), pp 7765-7781.
593 Chen, J., Chen, J., Liao, A., Cao, X., Chen, L., Chen, X., He, C., Han, G., Peng, S., Lu, M., Zhang, W., Tong, X., Mills, J., 2015.
594     Global land cover mapping at 30m resolution: A POK-based operational approach. ISPRS J. Photogramm. Remote Sens.,
595     Global Land Cover Mapping and Monitoring 103, 7–27. https://doi.org/10.1016/j.isprsjprs.2014.09.002
596 Chen, J., Li, C., Ristovski, Z., Milic, A., Gu, Y., Islam, M.S., Wang, S., Hao, J., Zhang, H., He, C. and Guo, H., 2017. A review of
597     biomass burning: Emissions and impacts on air quality, health and climate in China. Science of the Total Environment.
598 Du, H., Kong, L., Cheng, T., Chen, J., Du, J., Li, L., Xia, X., Leng, C. & Huang, G. 2011. Insights into summertime haze pollution
599     events over Shanghai based on online water-soluble ionic composition of aerosols. Atmospheric Environment, 45(29), pp
600     5131-5137.
601 Ellicott, E., Vermote, E., Giglio, L. and Roberts, G., 2009. Estimating biomass consumed from fire using MODIS FRE. Geophysical
602     Research Letters, 36(13).

603    Freeborn, P. H., Wooster, M. J., Hao, W. M., Ryan, C. A., Nordgren, B. L., Baker, S. P. & Ichoku, C. 2008. Relationships between
604        energy release, fuel mass loss, and trace gas and aerosol emissions during laboratory biomass fires. Journal of Geophysical
605        Research: Atmospheres, 113(D1), pp D01301.
606    Fu, J. Y., Jiang, D., Huang, Y. H., 2014a. 1-km grid population dataset of China, Global Change Research Data
607        Publishing & Repository, DOI:10.3974/geodb.2014.01.06.V1
608    Fu, J. Y., Jiang, D., Huang, Y. H., 2014b. 1-km grid GDP dataset of China, Global Change Research Data Publishing
609        & Repository, DOI:10.3974/geodb.2014.01.07.V1Gao, X., Ma, W., Ma, C., Zhang, F., Wang, Y., 2002. Analysis of the
610        current status of utilization of crop straw in China. Journal of Huazhong Agricultural University 21, 242–247 (in Chinese).
611    Giglio, L., Csiszar, I. & Justice, C. 2006. Global distribution and seasonality of active fires as observed with the Terra and Aqua
612        Moderate Resolution Imaging Spectroradiometer (MODIS) sensors. J. Geophys. Res, 111(G02016.
613    Giglio, L., Randerson, J.T. and Werf, G.R., 2013. Analysis of daily, monthly, and annual burned area using the fourth-generation
614        global fire emissions database (GFED4). Journal of Geophysical Research: Biogeosciences, 118(1), pp.317-328.
615    Goldberg, M.D., Kilcoyne, H., Cikanek, H., Mehta, A., 2013. Joint Polar Satellite System: The United States next generation
616        civilian polar-orbiting environmental satellite system. J. Geophys. Res. Atmospheres 118, 13,463-13,475.
617        https://doi.org/10.1002/2013JD020389
618    He, M., Zheng, J., Yin, S. & Zhang, Y. 2011. Trends, temporal and spatial characteristics, and uncertainties in biomass burning
619        emissions in the Pearl River Delta, China. Atmospheric Environment, 45(24), pp 4051-4059.
620    Huang, X., Li, M., Li, J. & Song, Y. 2012. A high-resolution emission inventory of crop burning in fields in China based on MODIS
621        Thermal Anomalies/Fire products. Atmospheric Environment, 50(0), pp 9-15.
622    Jiang, D., Zhuang, D., Fu, J., Huang, Y. & Wen, K. 2012. Bioenergy potential from crop residues in China: Availability and
623        distribution. Renewable and Sustainable Energy Reviews, 16(3), pp 1377-1382.
624    Kaiser, J. W., Heil, A., Andreae, M. O., Benedetti, A., Chubarova, N., Jones, L., Morcrette, J. J., Razinger, M., Schultz, M. G.,
625        Suttie, M. & van der Werf, G. R. 2012. Biomass burning emissions estimated with a global fire assimilation system based
626        on observed fire radiative power. Biogeosciences, 9(1), pp 527-554.
627    Li, W., Shao, L. & Buseck, P. 2010. Haze types in Beijing and the influence of agricultural biomass burning. Atmospheric
628        Chemistry and Physics, 10(17), pp 8119-8130.
629    Li, J.F. and Hu, Y.S., 2009. Analysis on investment and operation of straw-fired power plants in Jiangsu province. Electric power
630        technologic economics, 5, p.005 (in Chinese).
631    Li, J., Li, Y., Bo, Y. and Xie, S., 2016. High-resolution historical emission inventories of crop residue burning in fields in China
632        for the period 1990–2013. Atmospheric Environment, 138, pp.152-161.
633    Li, M., Zhang, Q., Kurokawa, J.I., Woo, J.H., He, K.B., Lu, Z., Ohara, T., Song, Y., Streets, D.G., Carmichael, G.R. and Cheng,
634        Y.F., 2015. MIX: a mosaic Asian anthropogenic emission inventory for the MICS-Asia and the HTAP projects. Atmos.
635        Chem. Phys. Discuss, 15(23), pp.34813-34869.
636    Liu, M., Song, Y., Yao, H., Kang, Y., Li, M., Huang, X. and Hu, M., 2015. Estimating emissions from agricultural fires in the
637        North China Plain based on MODIS fire radiative power. Atmospheric environment, 112, pp.326-334.
638    Liu, H., Jiang, G. M., Zhuang, H. Y. & Wang, K. J. 2008. Distribution, utilization structure and potential of biomass resources in
639        rural China: With special references of crop residues. Renewable and Sustainable Energy Reviews, 12(5), pp 1402-1418.
640    NBSC (National Bureau of Statistic of China) China Statistical Yearbook, 480 2003–2015, China Statistics Press, Beijing (2004–
641        2016) (in Chinese).
642    Portmann, F. T., Siebert, S. & Döll, P. 2010. MIRCA2000—Global monthly irrigated and rainfed crop areas around the year 2000:
643        A new high-resolution data set for agricultural and hydrological modeling. Global Biogeochemical Cycles, 24(1).
644    Qin, Y. & Xie, S. D. 2011. Historical estimation of carbonaceous aerosol emissions from biomass open burning in China for the
645        period 1990–2005. Environmental Pollution, 159(12), pp 3316-3323.
646    Randerson, J., Chen, Y., Werf, G., Rogers, B. & Morton, D. 2012. Global burned area and biomass burning emissions from small
647        fires. Journal of Geophysical Research: Biogeosciences (2005–2012), 117(G4), pp.
648    Roberts, G., Wooster, M.J. and Lagoudakis, E., 2009. Annual and diurnal african biomass burning temporal dynamics.
649        Biogeosciences, 6(5), pp.849-866.
650    Roberts, G., Wooster, M.J., Xu, W., Freeborn, P.H., Morcrette, J.J., Jones, L., Benedetti, A. and Kaiser, J., 2015. LSA SAF Meteosat
651        FRP Products: Part 2--Evaluation and demonstration of use in the Copernicus Atmosphere Monitoring Service (CAMS).
652        Atmospheric Chemistry & Physics Discussions, 15(12).
653    Schroeder, W., Oliva, P., Giglio, L. and Csiszar, I.A., 2014. The New VIIRS 375 m active fire detection data product: Algorithm
654        description and initial assessment. Remote Sensing of Environment, 143, pp.85-96.
655    Streets, D.G., Yarber, K.F., Woo, J.H. and Carmichael, G.R., 2003. Biomass burning in Asia: Annual and seasonal estimates and
656        atmospheric emissions. Global Biogeochemical Cycles, 17(4).
657    Sun, J., Peng, H., Chen, J., Wang, X., Wei, M., Li, W., Yang, L., Zhang, Q., Wang, W. & Mellouki, A. 2016. An estimation of
658        CO2 emission via agricultural crop residue open field burning in China from 1996 to 2013. Journal of Cleaner Production,
659        112, Part 4(2625-2631.
660    van der Werf, G. R., Randerson, J. T., Giglio, L., Collatz, G. J., Mu, M., Kasibhatla, P. S., Morton, D. C., DeFries, R. S., Jin, Y. &
661        van Leeuwen, T. T. 2010. Global fire emissions and the contribution of deforestation, savanna, forest, agricultural, and peat
662        fires (1997–2009). Atmos. Chem. Phys., 10(23), pp 11707-11735.

van der Werf, G. R., Randerson, J. T., Giglio, L., van Leeuwen, T. T., Chen, Y., Rogers, B. M., Mu, M., van Marle, M. J. E., Morton, D. C., Collatz, G. J., Yokelson, R. J., and Kasibhatla, P. S.: Global fire emissions estimates during 1997–2016, Earth Syst. Sci. Data, 9, 697-720, https://doi.org/10.5194/essd-9-697-2017, 2017.

Wang & Zhang, 2016, http://news.chengdu.cn/2016/1106/1829718.shtml,Chengdu Business Daily

Wang, S. & Zhang, C. 2008. Spatial and temporal distribution of air pollutant emissions from open burning of crop residues in China. Sciencepaper online, 3(5), pp 329-333.

Wolfe, R.E., Lin, G., Nishihama, M., Tewari, K.P., Tilton, J.C. and Isaacman, A.R., 2013. Suomi NPP VIIRS prelaunch and on-orbit geometric calibration and characterization. Journal of Geophysical Research: Atmospheres, 118(20), pp.11-508.

Wooster, M. J., Roberts, G., Perry, G. L. W. & Kaufman, Y. J. 2005. Retrieval of biomass combustion rates and totals from fire radiative power observations: FRP derivation and calibration relationships between biomass consumption and fire radiative energy release. Journal of Geophysical Research: Atmospheres, 110(D24), pp D24311.

Xu, W., Wooster, M.J., Kaneko, T., He, J., Zhang, T. and Fisher, D., 2017. Major advances in geostationary fire radiative power (FRP) retrieval over Asia and Australia stemming from use of Himarawi-8 AHI. Remote Sensing of Environment, 193, pp.138-149.

Yamaji, K., Li, J., Uno, I., Kanaya, Y., Irie, H., Takigawa, M., Komazaki, Y., Pochanart, P., Liu, Y., Tanimoto, H., Ohara, T., Yan, X., Wang, Z. & Akimoto, H. 2010. Impact of open crop residual burning on air quality over Central Eastern China during the Mount Tai Experiment 2006 (MTX2006). Atmos. Chem. Phys., 10(15), pp 7353-7368.

Yan, X., Ohara, T. & Akimoto, H. 2006. Bottom-up estimate of biomass burning in mainland China. Atmospheric Environment, 40(27), pp 5262-5273.

Yang, S., He, H., Lu, S., Chen, D. & Zhu, J. 2008. Quantification of crop residue burning in the field and its influence on ambient air quality in Suqian, China. Atmospheric Environment, 42(9), pp 1961-1969.

Za, 2015, http://www.chinanews.com/sh/2015/11-04/7606112.shtml, Legislative Evening Newspaper

Zhang, H., Ye, X., Cheng, T., Chen, J., Yang, X., Wang, L. & Zhang, R. 2008. A laboratory study of agricultural crop residue combustion in China: Emission factors and emission inventory. Atmospheric Environment, 42(36), pp 8432-8441.

Zhang, L., Liu, Y. and Hao, L., 2016. Contributions of open crop straw burning emissions to PM2. 5 concentrations in China. Environmental Research Letters, 11(1), p.014014.

Zhang, T., Wooster, M.J., Green, D.C. and Main, B., 2015. New field-based agricultural biomass burning trace gas, PM2. 5, and black carbon emission ratios and factors measured in situ at crop residue fires in Eastern China. Atmospheric Environment, 121, pp.22-34.

Zhang, T., Wooster, M.J. and Xu, W., 2017. Approaches for synergistically exploiting VIIRS I-and M-Band data in regional active fire detection and FRP assessment: A demonstration with respect to agricultural residue burning in Eastern China. Remote sensing of environment, 198, pp.407-424.

Zhang, T., Wooster, M., de Jong, M. and Xu, W., 2018. How Well Does the 'Small Fire Boost'Methodology Used within the GFED4. 1s Fire Emissions Database Represent the Timing, Location and Magnitude of Agricultural Burning?. Remote Sensing, 10(6), p.823.

Zhao, H., Tong, D. Q., Gao, C. & Wang, G. 2015. Effect of dramatic land use change on gaseous pollutant emissions from biomass burning in North Eastern China. Atmospheric Research, 153(429-436).

Zhou, L., Divakarla, M., Liu, X., Layns, A., Goldberg, M., 2019. An Overview of the Science Performances and Calibration/Validation of Joint Polar Satellite System Operational Products. Remote Sens. 11, 698. https://doi.org/10.3390/rs11060698

Zuo 2015, http://www.chinanews.com/gn/2015/12-11/7666514.shtml, Anhui News

705 **Table 1:** Emission Factors for agricultural residue burning used in this study. Wheat and rice emission factors were
706 derived from field measurements conducted in eastern China and reported by Zhang et al. (2015), while the corn
707 emission factors are from Andreae and Merlet (2001), the same as those used in GFAS (Kaiser *et al.,* 2012). *$PM_{2.5}$
708 = particulate matter with diameter < 2.5μm
709

| | Emissions Factor (g.kg$^{-1}$) | | |
|---|---|---|---|
| | Wheat | Corn | Rice |
| $CO_2$ | 1739±19 | 1308±14 | 1761±30 |
| CO | 60±12 | 92±18 | 47±19 |
| $PM_{2.5}$* | 6.1±1.3 | 8.3±1.8 | 9.6±4.3 |
| Black Carbon | 0.70±0.09 | 0.42±0.05 | 0.56±0.04 |

710
711 **Table 2:** Total species-specific fire emissions calculated in this study for agricultural burning in eastern China, and
712 comparison to those contained within other fire emissions inventories and calculated in previous studies.
713

| Reference | Region | Year | Method | Emissions (Gg.yr$^{-1}$) | | | |
|---|---|---|---|---|---|---|---|
| | | | | $CO_2$ | CO | $PM_{2.5}$ | BC |
| This study | Eastern China | 2012 | Satellite | 31066 ± 1960 | 1035±327 | 124±43 | 11±1.8 |
| | | 2013 | | 31107 ± 1748 | 1025±320 | 130±44 | 11±1.7 |
| | | 2014 | | 27069 ± 1421 | 904±279 | 107±36 | 10±1.5 |
| | | 2015 | | 16932 ± 1044 | 562±177 | 70±24 | 6±0.95 |
| GFAS | Eastern China | 2012 | Satellite | 9219 | 649 | 58 | 3.0 |
| Kaiser *et al.,* 2012 | | 2013 | | 8173 | 576 | 52 | 2.6 |
| | | 2014 | | 8760 | 617 | 55 | 2.8 |
| | | 2015 | | 6818 | 480 | 43 | 2.2 |
| GFED4.1s | Eastern China | 2012 | Satellite | 18629 | 1199 | 74 | 8.8 |
| Van der Werf *et al.*, 2017 | | 2013 | | 24034 | 1547 | 95 | 11 |
| | | 2014 | | 18241 | 1173 | 72 | 8.6 |
| | | 2015 | | 15892 | 1023 | 63 | 7.5 |
| Liu *et al.,* 2015 | NCP[1] | 2012 | Satellite | 26000 | 1700 | 102 | 13 |
| | | 2013 | | 9800 | 630 | 39 | 5 |
| | | 2014 | | 13000 | 820 | 50 | 6 |
| Zhang et al., 2008 | Eastern China[3] | 2004 | CYBA[2] | 67703 | 5624 | - | - |
| Huang et al., 2012 | Eastern China[3] | 2006 | CYBA | 41374 | 2668 | 164 | 20 |
| Qiu et al., 2016 | Eastern China | 2013 | CYBA | 72071 | 2549 | 445 | 42 |
| Li et al., 2016 | NCP | 2012 | CYBA | 68675 | 5983 | 452 | 23 |
| Sun et al., 2016 | China | 2013 | CYBA | 192540 | - | - | - |
| Street *et al.,* 2003 | China | 2000 | CYBA | 160000 | 10000 | - | 70 |
| Yan *et al.,* 2006 | China | 2000 | CYBA | 184000 | 11000 | 470 | 80 |

714 [1] NCP refers to the North China Plain, which has a geographic extent similar to that of this study (32-41°N, 113-121°E).
715 [2] CYBA refers to Crop Yield Based Approaches, see Section 2.6.1
716 [3] Sum of provinces/cities shown in Fig.1 of this study.
717
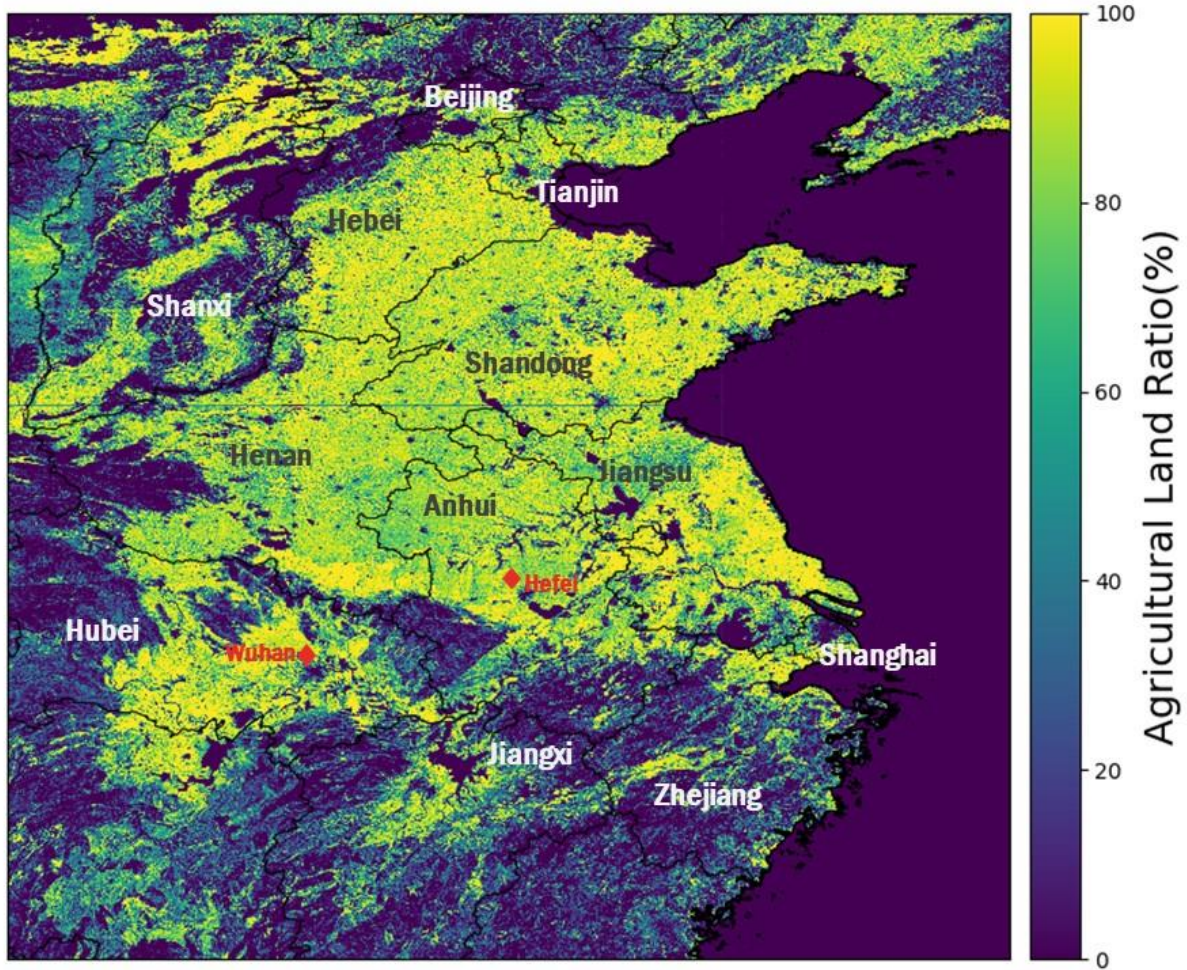
718
719 **Figure 1:** The spatial extent of the study area (111-123° E, 27-40° N). The agricultural land ratio taken from the
720 GlobeLand30 land cover product (Chen et al, 2015) was re-gridded to 0.01 degree spatial resolution, and is overlain
721 with the main provinces, mega-cities and some important provincial capital cities in eastern China. The basic layer of
722 country/province borders within this map was created using Python Basemap librabry.
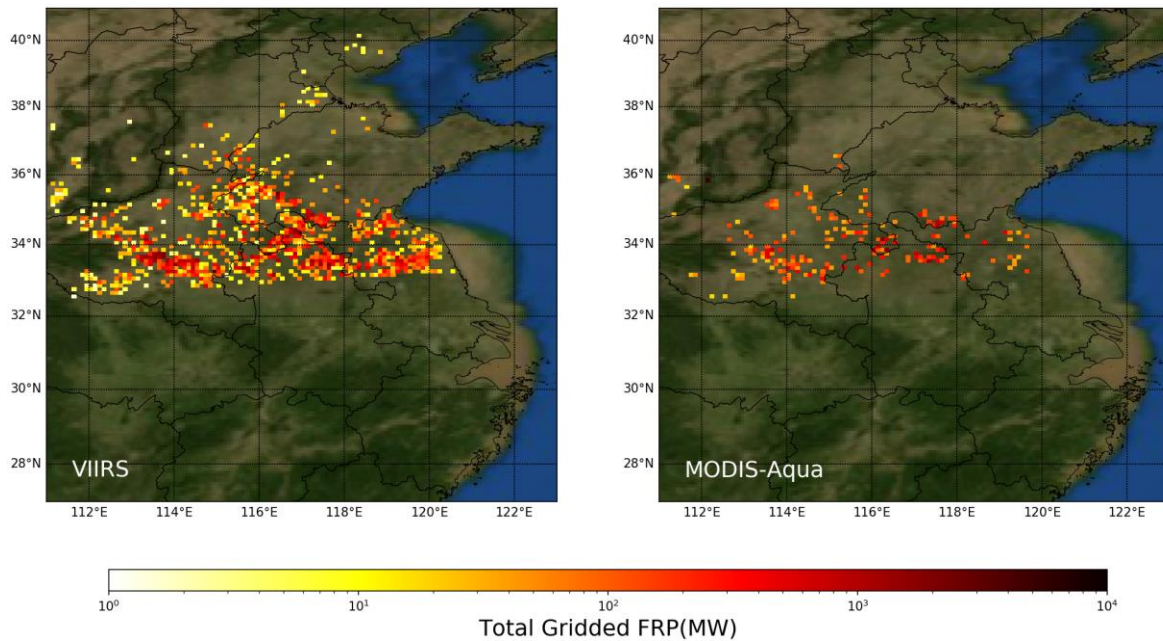
723
724 **Figure 2:** Example of the spatial distribution of total gridded FRP (MW; calculated per 0.1° grid cell) calculated from
725 near simultaneous VIIRS-IM and MODIS Aqua data collected over the eastern China study area of Fig. 1 on June
726 12th, 2012. The VIIRS-IM data product clearly quantifies a higher proportion of the FRP from fires burning in the
727 region at the time of the satellite overpass than MODIS Aqua does. The basic layer of country/province borders within
728 this map was created using Python Basemap librabry.
729
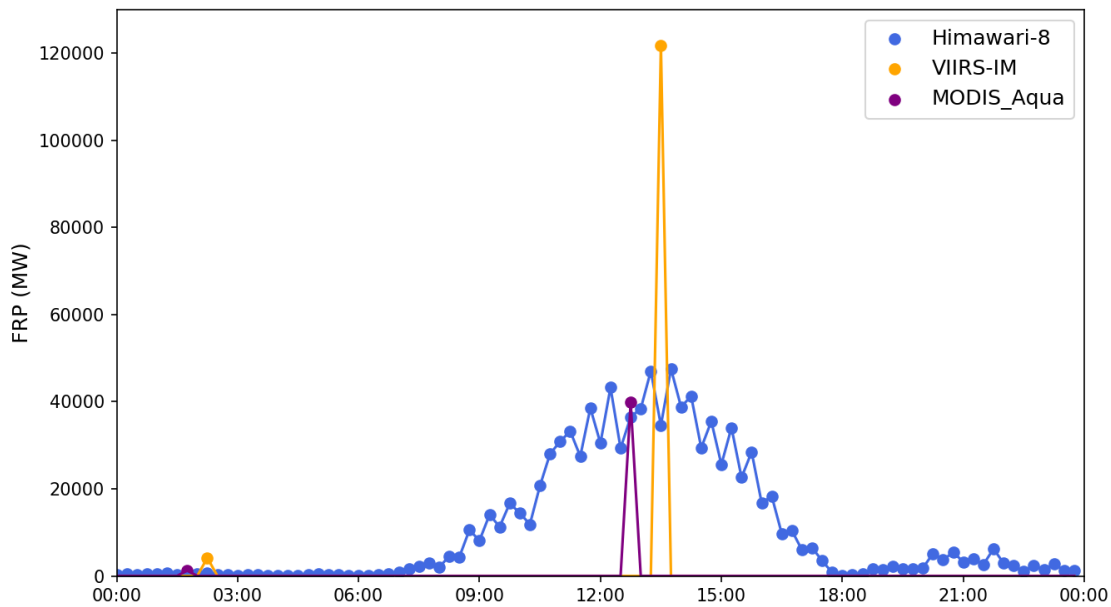
730
731 **Figure 3:** Time series of spatially summed FRP for eastern China, as retrieved from geostationary Himawari, and
732 polar-orbiting VIIRS-IM and MODIS observations made on June 11th, 2015. VIIRS and MODIS Aqua provide
733 typically two observations per day, and sometimes three when the swath overlaps from different orbits occur.
734 Himawari provides 144 observations per day.
735
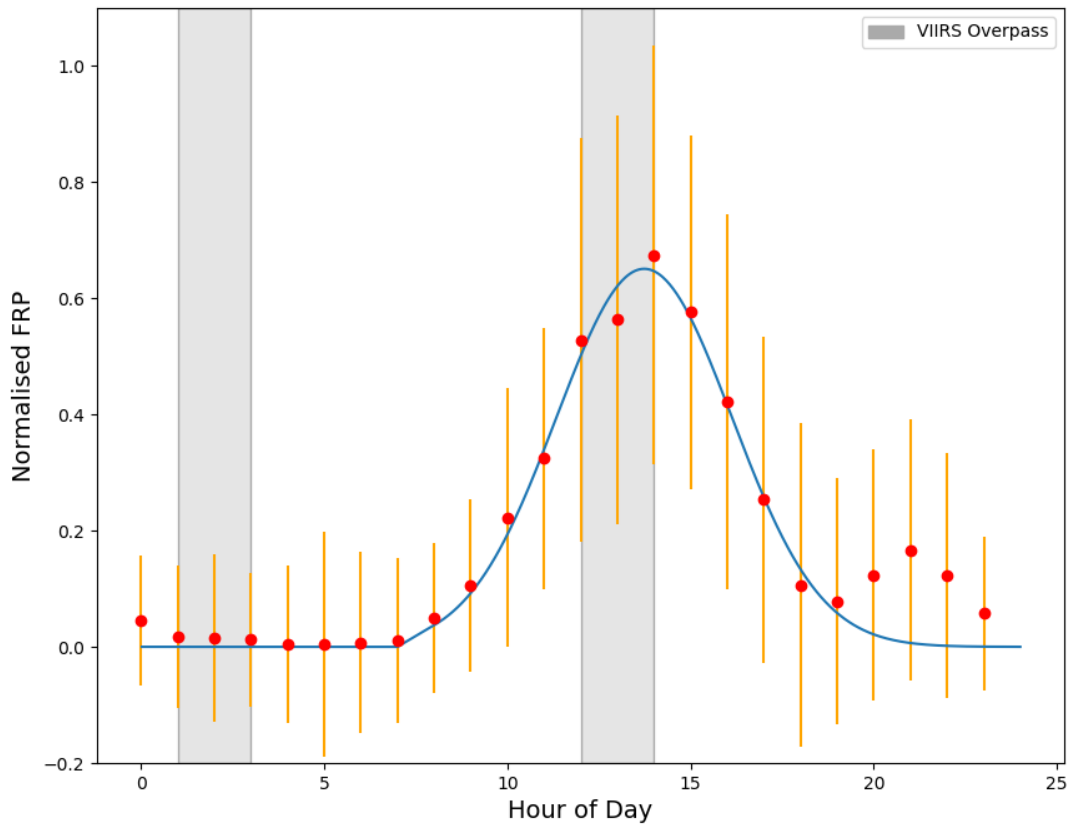
736
737 **Figure 4:** Time series of hourly normalised fire radiative power derived from Himawari-8 FRP data generated using
738 the algorithm of Xu et al. (2017) over eastern China at 0.1 degree for June 2015 (the 'Summer' diurnal fire cycle).
739 The blue curve shows the best fit of the Gaussian distribution, with orange error bar show standard deviation. Grey
740 shading shows the two daily VIIRS overpass periods.
741
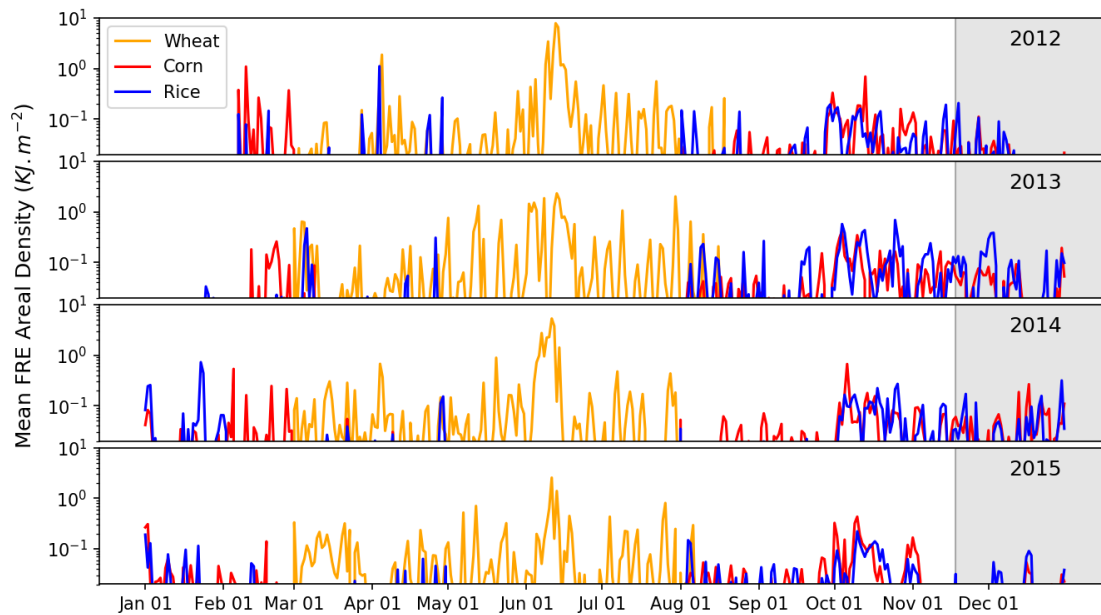
742
743 **Figure 5:** Time-series of mean daily FRE areal density (kJ m$^{-2}$, calculated per 0.1° grid cell) from 2012-2015 for the
744 entire study area disaggregated by crop residue type (wheat, corn and rice) according to the method described in
745 Section 2.4. Grey shaded areas highlighted the usual newly discovered winter burning season from mid-November to
746 December when no crop harvesting occurs but where fires are clearly occurring. This period of agricultural burning
747 is discussed further in Section 5.1
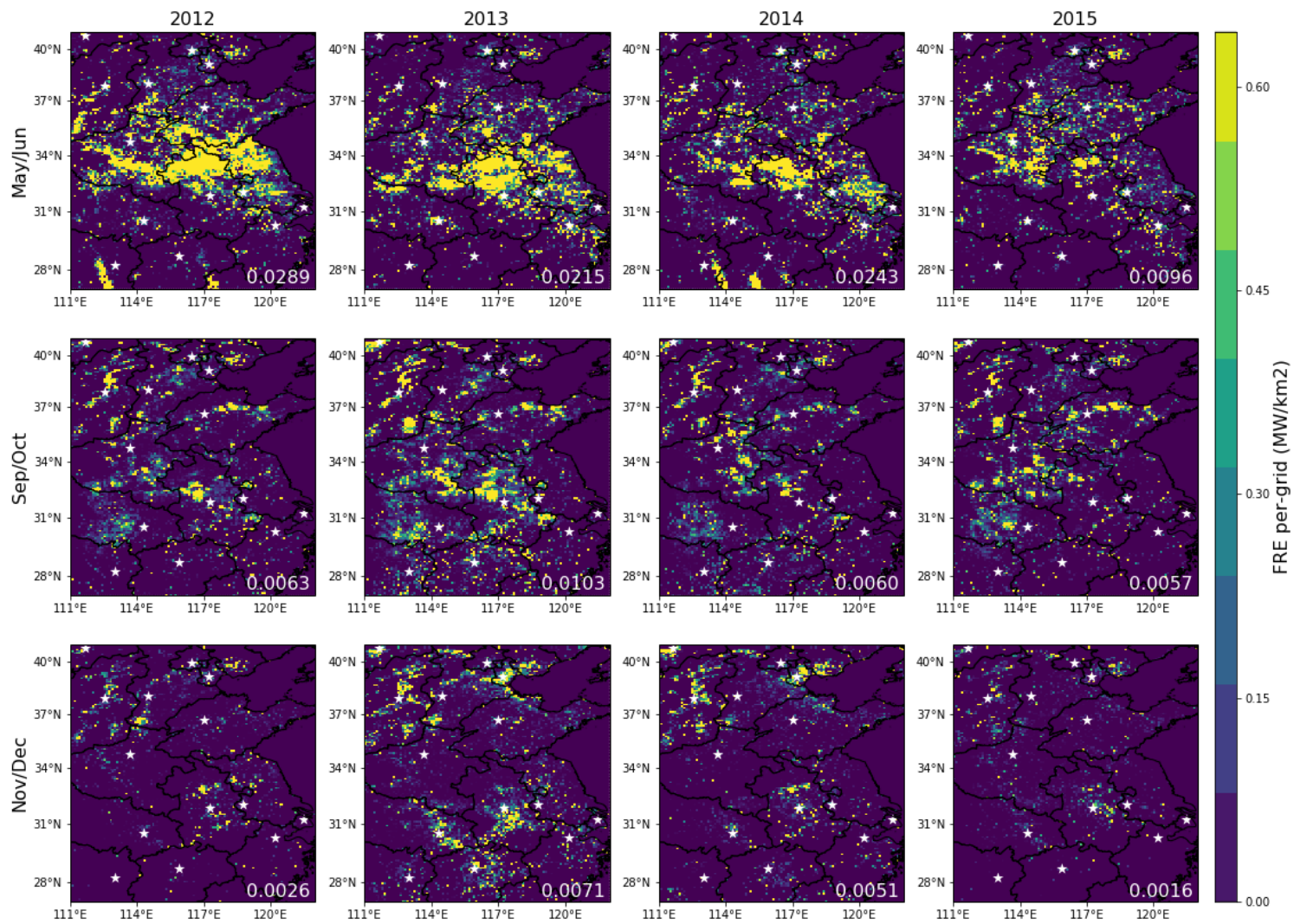
**Figure 6**: Spatial distribution of FRE areal density (MJ.m$^{-2}$, 0.1 deg grid cells) for agricultural fires in eastern China from 2012 to 2015 (top to bottom rows) split by fire season: summer (May-June, top row), autumn (Sep-Oct, middle row) and winter (Nov-Dec, bottom row). Mean regional FRE for each season is indicated

in white text, and the capital city location of each province is shown as a white star on each map. The basic layer of country/province borders within this map was created using Python Cartopy librabry.
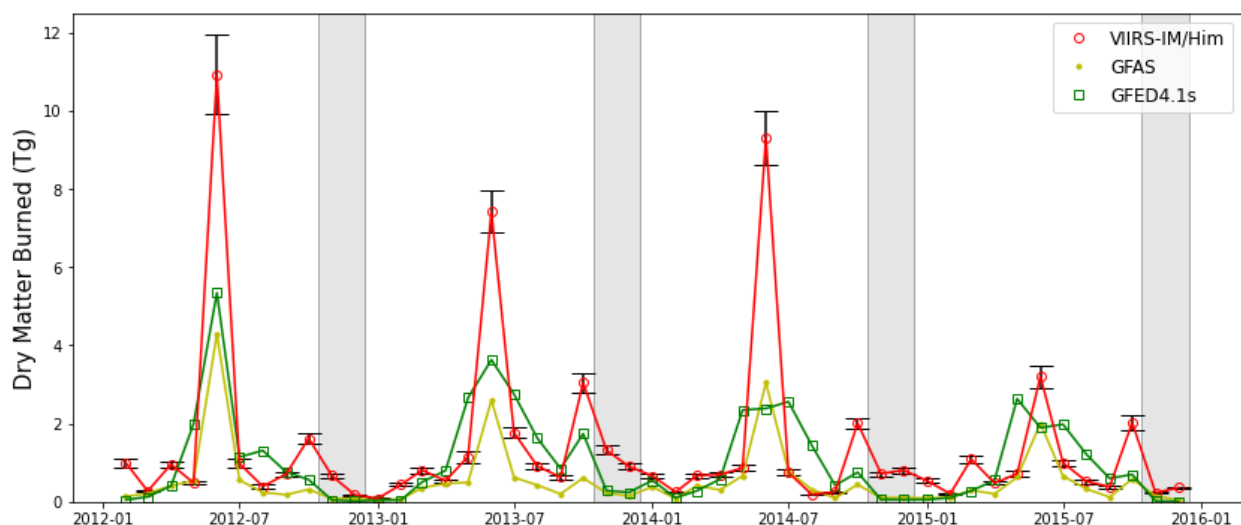
**Figure 7:** Monthly (2012-2015) time-series of total dry matter burned (DMB) retrieved using the VIIRS-IM/Him FRP product developed in this study (with standard deviation shown as black error bars), along with comparable GFAS and GFED4.1s DMB totals. Grey shaded areas highlighted the winter burning season from mid-November to December (Section 5.1).
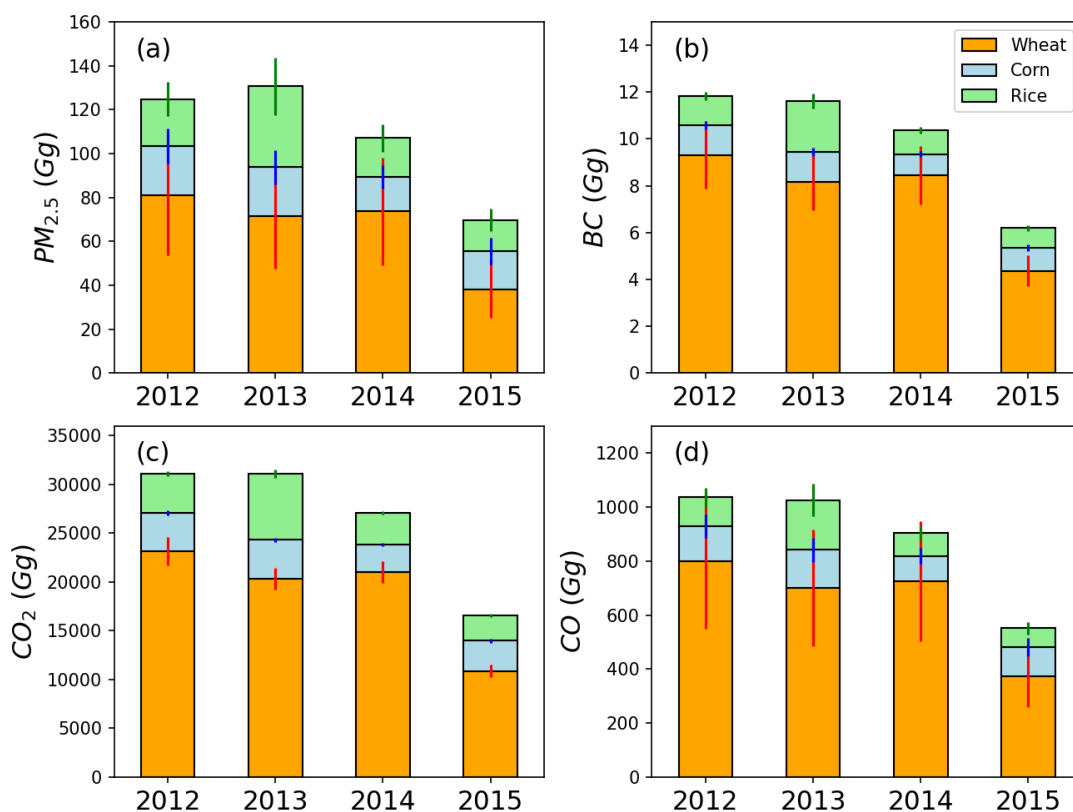
**Figure 8:** Annual total $PM_{2.5}$, BC, $CO_2$, and CO emissions for eastern China for the three main crop residues burning types (wheat, corn, rice) calculated for 2012-2015 using the VIIRS-IM/Him based emissions inventory developed herein. Coloured error bars indicate 1 standard deviation.
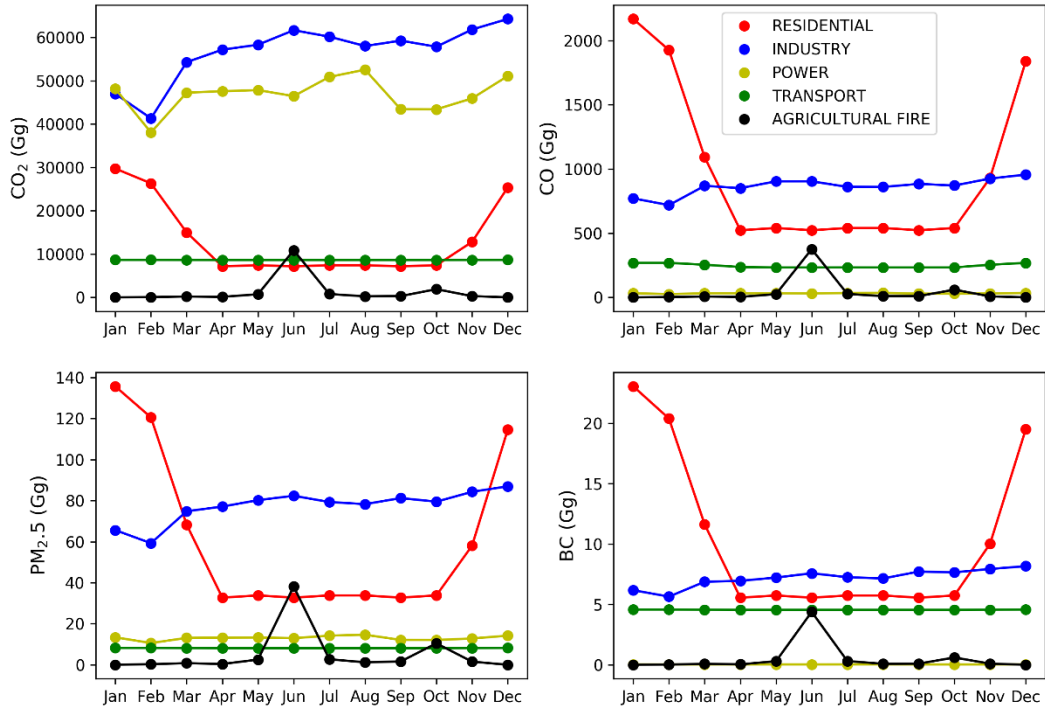
**Figure 9:** Comparison of monthly $CO_2$, CO, $PM_{2.5}$ and BC emissions from agricultural fires with those from other emission sources (residential, industry, power, transport, data source: Li et al., 2015) in the intensive burning area (32-36º N, 112-122º E) of eastern China in the year 2013.
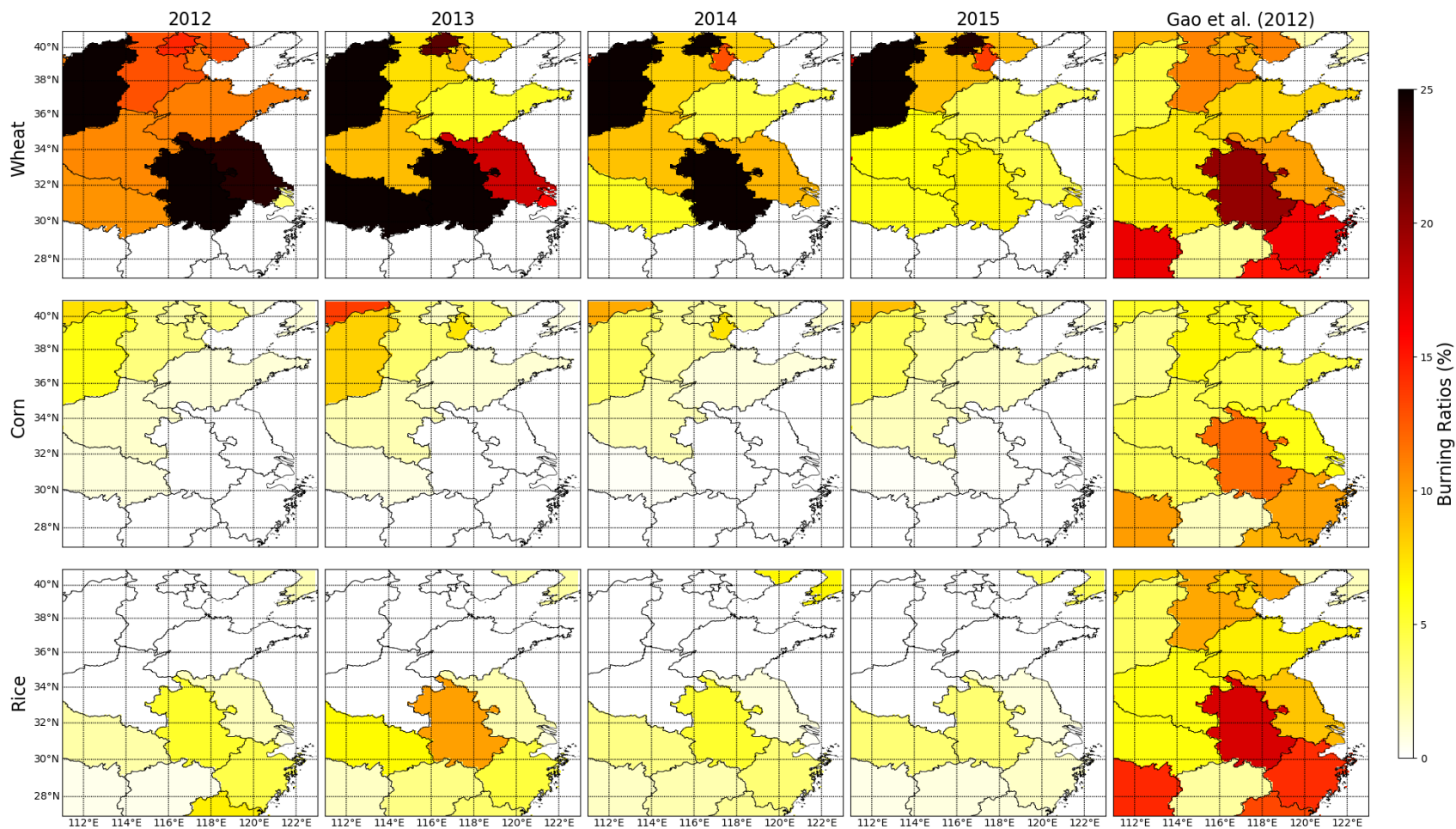
**Figure 10:** Temporal and spatial variability of province-specific percentages of crop residues burned in the fields (burning ratio metrics) of eastern China. Data are calculated using crop yield estimates from National Bureau of Statistics of China and the dry matter burned totals derived herein using our VIIRS-IM/Him DMB datasets from 2012-2015, and compared to the temporally invariant estimates provided by Gao et al., (2002, final column). The basic layer of country/province borders within this map was created using Python Basemap librabry.
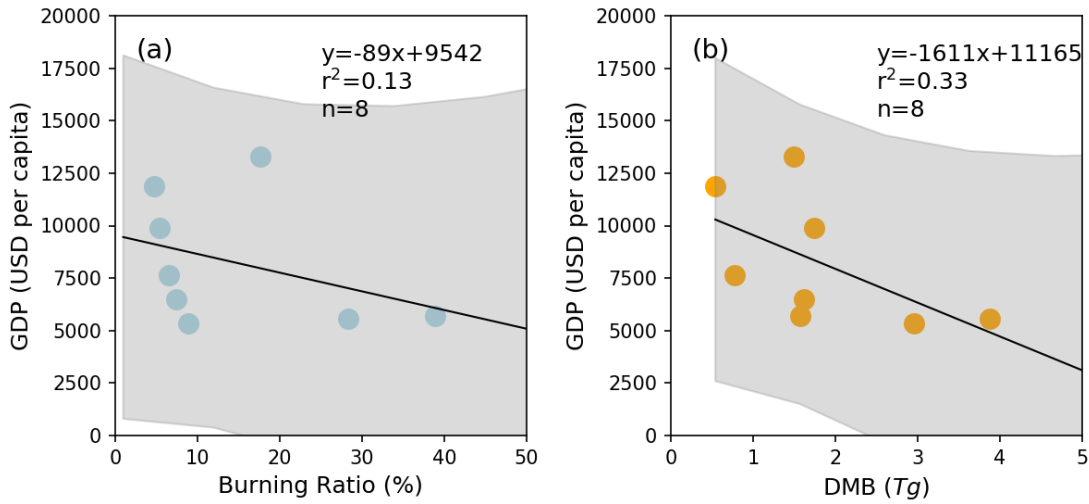
**Figure 11:** Direct comparisons of mean GDP per capita with (a) burning ratio for wheat from 2012, (b) province-specific yearly dry matter burned (DMB). The best fit linear relationships are shown, along with its equation, and the grey shaded area represents the 95% confidence limit on the relationship.
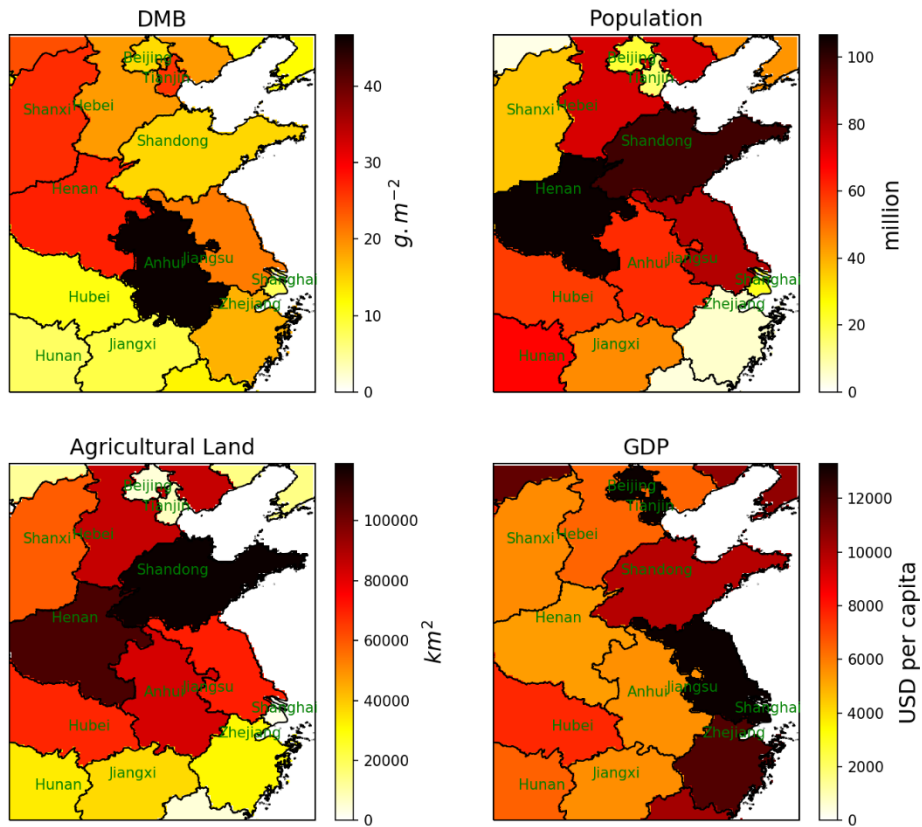
**Figure 12:** Spatial distribution of province-specific: (a) mean annual dry matter burned as calculated using the VIIRS-IM/Him approach developed herein, (b) population (Data source: Fu *et al.,* 2014a), (c) agricultural land area (Data source: GlobeLand30, http://www.globallandcover.com/) and (d) mean GDP per capita (Data source: Fu *et al.,* 2014b). The basic layer of country/province borders within this map was created using Python Basemap librabry.
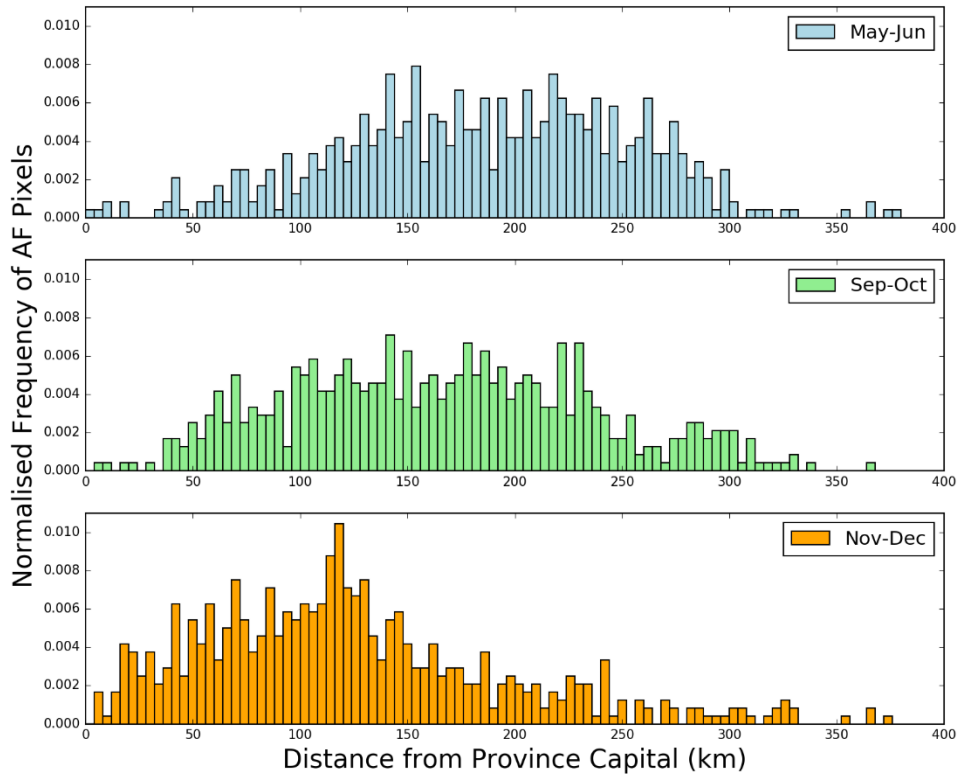
**Figure 13:** Normalised frequency distribution of distance from province capital of the top 10% of high FRE VIIRS-IM/Him product 0.1 degree grid cells during the three burning seasons: Summer - May to June (top, blue), Autumn – September to October (middle, green), and Winter - November to December (bottom, orange). A clear shift towards the origin can be observed in the Nov-Dec period compared with Sep-Oct.